



**HAL**  
open science

# A global reassessment of the controls on iron speciation in modern sediments and sedimentary rocks: A dominant role for diagenesis

V. Pasquier, D. A. Fike, S. Révillon, I. Halevy

## ► To cite this version:

V. Pasquier, D. A. Fike, S. Révillon, I. Halevy. A global reassessment of the controls on iron speciation in modern sediments and sedimentary rocks: A dominant role for diagenesis. *Geochimica et Cosmochimica Acta*, 2022, 335, pp.211-230. 10.1016/j.gca.2022.08.037 . insu-03868828

**HAL Id: insu-03868828**

**<https://insu.hal.science/insu-03868828>**

Submitted on 18 Mar 2023

**HAL** is a multi-disciplinary open access archive for the deposit and dissemination of scientific research documents, whether they are published or not. The documents may come from teaching and research institutions in France or abroad, or from public or private research centers.

L'archive ouverte pluridisciplinaire **HAL**, est destinée au dépôt et à la diffusion de documents scientifiques de niveau recherche, publiés ou non, émanant des établissements d'enseignement et de recherche français ou étrangers, des laboratoires publics ou privés.



Distributed under a Creative Commons Attribution 4.0 International License



Contents lists available at ScienceDirect

## Geochimica et Cosmochimica Acta

journal homepage: [www.elsevier.com/locate/gca](http://www.elsevier.com/locate/gca)

# A global reassessment of the controls on iron speciation in modern sediments and sedimentary rocks: A dominant role for diagenesis

V. Pasquier<sup>a,\*</sup>, D.A. Fike<sup>b</sup>, S. Révillon<sup>c</sup>, I. Halevy<sup>a</sup><sup>a</sup> Earth and Planetary Sciences, Weizmann Institute of Science, Rehovot, Israel<sup>b</sup> Earth and Planetary Sciences, Washington University in St. Louis, St. Louis, MO, USA<sup>c</sup> SEDISOR, Institut Universitaire Européen de la Mer, Plouzané, France

## ARTICLE INFO

## Article history:

Received 1 November 2021

Accepted 29 August 2022

Available online 5 September 2022

Associate editor: Alexandra V. Turchyn

## Keywords:

Iron speciation

Water-column chemistry and oxygenation state

Porewater chemistry

Early diagenesis

Iron speciation in sediment sources

## ABSTRACT

The speciation of iron in sediments and sedimentary rocks is a widely used proxy for the chemistry and oxidation state of ancient water bodies. Specifically, the fraction of reactive iron out of the total iron ( $Fe_{HR}/Fe_T$ ) and the fraction of pyrite iron out of the reactive iron pool ( $Fe_{PYR}/Fe_{HR}$ ) are thought to constrain the oxidation state and the presence of sulfide in the water column, respectively. This approach was developed and tested against modern core-top sediments, but application to sedimentary rocks requires consideration of the effects of diagenesis and lithification on iron speciation. Furthermore, the effects of deep burial, metamorphism, and late-stage alteration during exhumation or sampling (e.g., oxidative weathering) have not been systematically explored. To bridge this gap, we combined new data from four sediment cores ( $n = 54$ ) with an extensive literature compilation of modern sediments (2936 measurements from 316 cores) and ancient sedimentary rocks (12,173 measurements spanning the Neoproterozoic to Quaternary). The modern data include both surface and buried sediments, allowing an investigation of the effects of diagenesis on iron speciation. Depending on the thresholds used to distinguish oxic from anoxic environments and ferruginous from euxinic environments, interpretation of the modern sedimentary iron speciation data within the existing framework yields incorrect environmental classifications up to  $\approx 70\%$  of the time. In modern sediments, diagenesis is the main reason that iron speciation does not represent the chemistry and oxidation state of the water column. We find that iron speciation correlates with porewater chemistry and that it changes with progressive burial along three distinctive  $Fe_{HR}/Fe_T - Fe_{PYR}/Fe_{HR}$  arrays, each of which represents a different set of diagenetic processes. We suggest that similarly to modern sediments, stratigraphic variation in iron speciation in sedimentary rocks primarily reflects progressive burial diagenesis or variation in depositional conditions rather than temporal variation in water-column chemistry and oxidation state. Indeed, analysis of the geologic iron speciation data reveals no statistically significant trends in either  $Fe_{HR}/Fe_T$  or  $Fe_{PYR}/Fe_{HR}$  from the Archean to the present day. The diagenetic  $Fe_{HR}/Fe_T - Fe_{PYR}/Fe_{HR}$  arrays that we identified in modern marine sediments suggest that under certain conditions, iron speciation analyses may be used to constrain  $Fe_{HR}/Fe_T$  in the local sediment source(s). Hence, we suggest that iron speciation data, together with complementary petrographic, mineralogical and geochemical constraints, may be used to constrain the local iron source(s) and early and late diagenetic processes, but rarely the chemistry or oxidation state of ancient water columns.

© 2022 The Authors. Published by Elsevier Ltd. This is an open access article under the CC BY license (<http://creativecommons.org/licenses/by/4.0/>).

## 1. Introduction

With few exceptions, iron (Fe) is present in most marine sediments at concentrations between 0 and  $\approx 10$  wt% (e.g., Clarkson et al., 2014; Hardisty et al., 2018; Raiswell and Canfield, 1998). In these sediments, Fe is sourced from riverine or wind-blown

particles, which are the products of continental weathering (e.g., Lu et al., 2017; Poulton and Raiswell, 2002; Raiswell et al., 2006). The sensitivity of secondary Fe mineralogy to the oxidation state and chemistry of aqueous environments (e.g., the concentration of dissolved inorganic carbon and/or sulfide) has prompted the use of the relative abundances of Fe(II)- and/or Fe(III)-bearing minerals to constrain these environmental parameters. For example, the presence or absence of Fe(II) carbonates in paleosols has been used to constrain Precambrian atmospheric  $CO_2$  levels

\* Corresponding author.

E-mail address: [virgil.pasquier@weizmann.ac.il](mailto:virgil.pasquier@weizmann.ac.il) (V. Pasquier).

(e.g., Kanzaki and Murakami, 2015; Sheldon, 2006), whereas Fe loss (as dissolved  $\text{Fe}^{2+}$ ) or retention (as Fe(III) minerals) in paleosols has been used to constrain atmospheric  $\text{O}_2$  levels (e.g., Sheldon et al., 2021). In another example, the ratios of Fe(III) to total Fe in altered oceanic crust have been used to document a Paleozoic increase in the  $\text{O}_2$  concentration of the deep ocean (Stolper and Keller, 2018).

In addition to the aforementioned Fe-based proxies for atmospheric and oceanic composition and oxidation state, indices of Fe mineralogy in sediments (e.g., the degree of pyritization, DOP) have been developed and used to reconstruct the oxidation state and chemistry of local water masses immediately overlying the sediment, and to study the controls on the formation of sedimentary pyrite in modern sediments (Berner, 1964, 1984; Canfield and Berner, 1987; Raiswell and Berner, 1986). To account for extensive observational and experimental evidence for a range of reactivity of Fe-bearing minerals towards sulfide (Anderson and Raiswell, 2004; Canfield et al., 1996; Lyons, 1996; Lyons and Severmann, 2006; Poulton and Raiswell, 2002; Raiswell and Canfield, 1998; Scholz, 2018; Wijsman et al., 2001), these approaches were refined to operationally classify Fe in sediments according to its reactivity towards sulfide. Hence, presently applied Fe classification schemes have converged on the quantification of the highly reactive to total Fe ratio ( $\text{Fe}_{\text{HR}}/\text{Fe}_{\text{T}}$ ) and the pyrite to highly reactive Fe ratio ( $\text{Fe}_{\text{PYR}}/\text{Fe}_{\text{HR}}$ ). This “Fe speciation” proxy for water-column chemistry and oxidation state has evolved over the years (please refer to Raiswell and Canfield, 2012; Raiswell et al., 2018 for a complete history), which may complicate comparison of reconstructions of modern and ancient settings made since this proxy was developed. Common to all iterations of this approach is that they have been based on the differential reactivity of Fe phases towards sulfide and the ability to extract and quantify these different Fe phases.

Surficial marine sediments are generally characterized by spatially-varying Fe concentrations of a few weight percent, either in dissolved forms (free  $\text{Fe}^{2+}$  and organic and inorganic complexes of Fe(II) and Fe(III)) or as fine-grained Fe (oxyhydr)oxides, all of which react rapidly with dissolved sulfide to form pyrite (Berner, 1984). Aqueous sulfide will be scavenged from sediment porewaters as long as sufficient amounts of dissolved and reactive particulate Fe species exist. Once these pools are exhausted, and even though the sediment may still contain abundant Fe in less reactive minerals (mostly Fe-bearing silicates), dissolved sulfide can start to accumulate in the porewater. Based on laboratory experiments, Canfield et al. (1992) estimated the rate constants for reaction of Fe-bearing minerals with 1 mM dissolved sulfide. The dataset shows a clear reactivity difference between the (oxyhydr)oxides (i.e., lepidocrocite, ferrihydrite, goethite and hematite), which have half-lives of hours to hundreds of days, and Fe-bearing silicate minerals, which are characterized by half-lives of up to 84,000 years (Canfield et al., 1992; Raiswell and Canfield, 1996). More recent experiments have verified these findings and refined the dependence of the mineral half-lives on the sulfide and dissolved organic matter concentrations, the mineral grain size, and the solution pH (Heitmann and Blodau, 2006; Hellige et al., 2012; Peiffer et al., 2015; Peiffer and Gade, 2007; Poulton et al., 2004; Wan et al., 2017; Wan et al., 2014).

Most recent studies rely on selective leaching protocols that relate chemically mobilized Fe to specific mineral fractions characterized by different reactivity towards sulfide (Hepburn et al., 2020 for a recent review). In a study that forms the basis of modern Fe speciation schemes, Poulton and Canfield (2005) used powdered synthetic minerals and measured the proportions of Fe extracted in eight steps. Four steps are applied sequentially to one aliquot

of sediment, targeting Fe phases that react to form pyrite and other Fe sulfides (e.g., mackinawite, troilite, pyrrhotite, marcasite, greigite) on timescales relevant to early diagenesis (Canfield et al., 1992): (1) sodium acetate targets iron carbonates, (2) hydroxylamine-HCl mixtures target easily reducible Fe(III) (oxyhydr)oxides (including ferrihydrite and lepidocrocite), (3) sodium dithionite targets Fe(III) (oxyhydr)oxides such as goethite, hematite, and akagenite, (4) ammonium oxalate targets magnetite ( $\text{Fe(II)Fe(III)}_2\text{O}_4$ ). A fifth step is applied to the same aliquot of sediment to extract the “poorly reactive” Fe ( $\text{Fe}_{\text{PRS}}$ ): (5) boiling HCl targets the Fe not extracted in steps 1–4. One or two additional steps are usually applied to a second aliquot of sediment, to determine the abundance of Fe sulfide phases: (6) reaction with strong HCl solutions at room temperature targets acid-volatile sulfur species, such as mackinawite-like phases, greigite or pyrrhotite, (7) chromium reduction targets all Fe sulfides, and elemental sulfur. Under the assumption that metastable acid-volatile sulfur species do not survive diagenesis and lithification, most ( $\approx 85\%$ ) Fe speciation studies of sedimentary rocks perform only the chromium reduction step. An eighth, full digestion step is sometimes applied to a third aliquot of sediment: (8) HCl- $\text{HNO}_3$ -HF mixtures target all Fe phases. The sum of steps 6 and 7 gives  $\text{Fe}_{\text{PYR}}$ , the sum of steps 1–4 and 6–7 gives  $\text{Fe}_{\text{HR}}$ , step 5 gives  $\text{Fe}_{\text{PRS}}$ . Quantification of  $\text{Fe}_{\text{T}}$  is achieved either by step 8 or by the sum of steps 1–7.

Recent exploration of the fidelity of the Poulton and Canfield (2005) extraction protocol using complementary analyses (e.g., magnetism, Mössbauer spectroscopy) has raised concerns regarding the ability of this protocol to extract the targeted phases in synthetic samples (pure and mixture), modern sediments and sedimentary rock samples (e.g., Hepburn et al., 2020; Slotznick et al., 2020). For example, the completeness of dissolution of carbonate-associated Fe in step 1 appears to be highly dependent on the abundance, grain size and mineralogy of these phases. When incomplete, the residual carbonate-associated Fe is leached in steps 2 to 4. Additionally, Fe(III) (oxyhydr)oxides, magnetite, some Fe sulfides (not pyrite) and/or  $\text{Fe}_{\text{PRS}}$  (e.g., berthierine and chamosite) are sometimes prematurely removed relative to the operationally defined scheme. Although it was concluded that the overall sequential leaching protocol is generally suitable for extraction and quantification of  $\text{Fe}_{\text{HR}}$  in sedimentary rocks (Hepburn et al., 2020; Slotznick et al., 2020), it was noted that (i) a specific Fe mineralogy should not be attributed to any of the operationally defined steps, and (ii) some  $\text{Fe}_{\text{PRS}}$  may be integrated into the  $\text{Fe}_{\text{HR}}$  pool, thereby increasing  $\text{Fe}_{\text{HR}}/\text{Fe}_{\text{T}}$  ratios and influencing reconstructions of the chemistry or oxidation state of past water columns.

The above nuances notwithstanding, decades of work on the behavior of Fe in modern sediments underpin the observation that the  $\text{Fe}_{\text{HR}}/\text{Fe}_{\text{T}}$  ratio, also known as the indicator of anoxicity, tracks water-column redox (Raiswell and Canfield, 1998; Raiswell and Canfield, 2012; Raiswell et al., 2018). According to Poulton and Raiswell, 2002,  $\text{Fe}_{\text{HR}}/\text{Fe}_{\text{T}} \leq 0.38$  (representing the extreme upper values for oxic Phanerozoic shales) are maintained in sediments underlying oxygenated water columns (Fig. 1A). In contrast, values above this threshold are commonly found when anoxic conditions (ferruginous or euxinic) develop and persist. Phanerozoic shales ( $n = 152$ ) deposited from oxic seawater display mostly  $\text{Fe}_{\text{HR}}/\text{Fe}_{\text{T}} \leq 0.22$  (average  $0.14 \pm 0.08 \sigma$ ), a lower threshold than modern sediments (Poulton and Raiswell, 2002). Based on these modern and ancient thresholds (Fig. 1A), sedimentary rocks have been classified as having deposited in clearly anoxic ( $\text{Fe}_{\text{HR}}/\text{Fe}_{\text{T}} > 0.38$ ), clearly oxic ( $\text{Fe}_{\text{HR}}/\text{Fe}_{\text{T}} \leq 0.22$ ) or intermediate ( $0.22 < \text{Fe}_{\text{HR}}/\text{Fe}_{\text{T}} \leq 0.38$ ) conditions. It has been suggested that

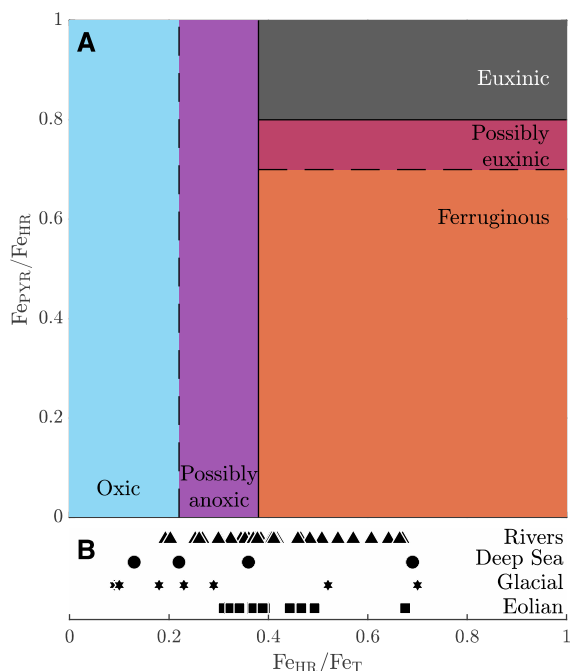


**Fig. 1.** Existing Fe speciation interpretive framework. **A.** Proposed diagnostic fields for water column chemistry and oxidation state (Poulton and Canfield, 2011). Solid lines are recommended boundaries for modern environments and dashed are suggested boundaries for ancient sediments (Raiswell et al., 2018). **B.** Present-day  $Fe_{HR}/Fe_T$  values of Fe inputs, where triangles show reported river suspended sediment (Poulton and Raiswell, 2002), circles represent deep-sea red clays (Poulton and Raiswell, 2002), stars represent sediments suspended in glacial meltwater (Raiswell et al., 2006), and squares represent aeolian dust (Lu et al., 2017; Poulton and Raiswell, 2002).

intermediate  $Fe_{HR}/Fe_T$  values may still reflect anoxic conditions, but in these cases, water column Fe enrichments may be masked by rapid sedimentation (e.g., in turbidites, Lyons and Severmann, 2006; Raiswell and Canfield, 1998), or the  $Fe_{HR}$  pool may have been depleted due to conversion of reactive Fe to less reactive Fe-bearing sheet silicates during diagenesis or metamorphism (reviewed in Slotznick et al., 2018a).

By considering the extent to which  $Fe_{HR}$  is converted to pyrite, as reflected by the  $Fe_{PYR}/Fe_{HR}$  ratio, ferruginous conditions may be distinguished from euxinic conditions (Fig. 1A; Raiswell and Canfield, 2012; Raiswell et al., 2018). Based on modern observations,  $Fe_{PYR}/Fe_{HR} > 0.8$  in sediments deposited under euxinic waters (e.g., Black Sea; Anderson and Raiswell, 2004; Raiswell and Canfield, 2012). Other studies have suggested a decrease of the  $Fe_{PYR}/Fe_{HR}$  threshold to 0.7 for distinguishing ferruginous from euxinic conditions for the Cretaceous Ocean Anoxic Event (OAE) 3 (März et al., 2008) and 0.6 for the Quaternary Mediterranean Sapropelic Events S5 and S7 (Benkovitz et al., 2020).

Deviations from the suggested Fe speciation systematics are known to exist, owing to changes in sediment porewater chemistry associated with microbial and abiotic reduction/oxidation (redox) reactions (Aller, 2014; Egger et al., 2015a; Egger et al., 2016; Egger et al., 2015b; Hutchings and Turchyn, 2021; Li et al., 2019; Liu et al., 2020; Ma et al., 2018; Scholz et al., 2014a; Scholz et al., 2019; Scholz et al., 2014b). By changing the oxidation state of Fe in the sediments, these redox reactions often drive mineral dissolution (e.g., reductive dissolution of Fe(III) (oxyhydr)oxides; Peiffer et al., 2015; Wan et al., 2017) and precipitation (e.g., pyrite, the Fe(II) phosphate vivianite, and Fe(II) carbonate; Lenstra et al., 2020; Vuillemin et al., 2019). These processes, collectively termed diagenesis, affect  $Fe_{HR}/Fe_T$  and  $Fe_{PYR}/Fe_{HR}$  ratios presumably inherited from the water column. For instance, when sulfide pools in

sediment porewater, modern observations reveal  $Fe_{PYR}/Fe_{HR}$  ratios that extend to values  $>0.7$  in sediments deposited under an oxic water column (Canfield, 1989; Canfield et al., 1992; Hardisty et al., 2018; Liu et al., 2020; Meister et al., 2019; Scholz et al., 2014b). In the case of  $Fe_{HR}/Fe_T$  ratios, the fragmented knowledge of diagenetic deviations from water-column values leads to many investigations that are conducted under the assumption of a constant  $Fe_{HR}/Fe_T$  ratio with burial. Additionally, an assumption implicit in many studies is that  $Fe_{HR}/Fe_T$  ratios are inherently rooted to the uppermost values of Phanerozoic shales of 0.38 (Poulton and Raiswell, 2002). However, rivers and abyssal surficial sediment can deviate considerably from this value (Fig. 1B), covering a range between  $\approx 0.2$  and  $\approx 0.7$  (Poulton and Raiswell, 2002). In this framework, any values higher than 0.38 would be erroneously interpreted to reflect ferruginous conditions. In the case of  $Fe_{PYR}/Fe_{HR}$ , sediments deposited under an oxic water column may show significant variation of porewater chemistry and Fe speciation with depth. For example,  $Fe_{PYR}/Fe_{HR}$  ratios of 0.00 to 0.93 have recently been reported in the Bornholm basin (Liu et al., 2020). As mentioned above, sulfide accumulation in porewater strongly affects the  $Fe_{PYR}/Fe_{HR}$  ratio, irrespective of the seawater redox state. The above deviations all suggest that early diagenetic processes or variation in the depositional conditions may strongly impact Fe speciation-based water-column chemistry and redox reconstructions.

The shortcomings of Fe speciation-based reconstructions of ancient seawater chemistry and redox stem in part from inherent differences between modern sedimentary and ancient geologic Fe speciation data. The interpretive framework of  $Fe_{HR}/Fe_T$  and  $Fe_{PYR}/Fe_{HR}$  ratios arises from extensive studies of surficial sediments (mostly 0–0.5 m below the sediment surface) in well-constrained environments, and this has allowed discussion of specific local controls on Fe speciation (e.g., Aller et al., 2010; Aquilina et al., 2014; Ma et al., 2018; Scholz et al., 2019). In contrast, geologic Fe speciation data come from sedimentary sequences that most commonly represent accumulation and progressive burial of sediments. Any point within such sequences is expected to have traversed through a range of depths below the ancient sediment–water interface as it got progressively buried. As such, these sequences are expected to record the variations in  $Fe_{HR}/Fe_T$  and  $Fe_{PYR}/Fe_{HR}$  ratios associated with, e.g., redox reactions, sulfide accumulation, and mineral dissolution/precipitation, as discussed above. This questions the utility of  $Fe_{HR}/Fe_T$  and  $Fe_{PYR}/Fe_{HR}$  ratios in the existing framework for constraining water-column chemistry and redox (e.g., Eroglu et al., 2021; Hutchings and Turchyn, 2021). Furthermore, the exact depositional context of geologic Fe speciation data is sometimes overlooked. The depositional context is crucial for evaluating the effects on Fe speciation of, e.g., the weathered lithology contributing to local Fe inputs, the organic carbon loading, and the deposition rate (e.g., Ahm et al., 2017).

Given the above, it appears that an understanding of the controls on Fe speciation requires consideration of modern sediments to a greater depth than 0.5 m below the sediment–water interface, and in the context of their depositional environment. Here, we compiled, curated, and reassessed published and newly measured Fe speciation data from modern marine sediments. This global compilation was used to identify the factors governing modern  $Fe_{HR}/Fe_T$  and  $Fe_{PYR}/Fe_{HR}$  ratios. Specifically, we attempted to address the following questions: How do  $Fe_{HR}/Fe_T$  and  $Fe_{PYR}/Fe_{HR}$  vary with seawater oxygenation, porewater chemistry, water depth, geographic location, and depositional environment? What is the original variability in  $Fe_{HR}/Fe_T$  and  $Fe_{PYR}/Fe_{HR}$  at the sediment–water interface, and how do post-depositional processes affect the original ratios? How does knowledge related to the above questions affect interpretations of Fe speciation-based paleo-reconstructions?

## 2. Materials and methods

### 2.1. Materials

Below we describe the materials analyzed in this study, which include a comprehensive compilation of existing Fe speciation data ( $n = 15,109$ ) and new data ( $n = 54$ ). The new data come from two drill cores in different and well understood modern depositional settings, and we present these together with previously published data from two other drill cores in well understood sites. The data from these four sites, which are described below, offer an opportunity to study the different environmental controls on the evolution of  $Fe_{HR}/Fe_T$  and  $Fe_{PYR}/Fe_{HR}$  ratios during early diagenesis.

#### 2.1.1. New Zealand

We selected a total of 42 samples (26 new and 16 previously reported by Pasquier et al., 2021a) from shelf and basin settings in the East New Zealand (ENZOSS) sedimentary system, from boreholes drilled by the International Ocean Discovery Program Leg 317 – site 1352 (44.9374°S, 172.022692°W, 344 m water depth) and Ocean Drilling Program (ODP) Leg 181 – site 1123 (41.786°S, 171.499°W, 3290 m water depth). Despite their proximity and contemporaneous deposition, these two records preserve radically different pyrite sulfur isotope compositions ( $\delta^{34}S_{PYR}$ ), which result from differences between the shallow and deep depositional environments (e.g., distance from land and sedimentation rate) over the last 40 Myr (Pasquier et al., 2021a). Of the 42 samples, 26 are first reported in the present study and come from borehole U1352, east of the southern island of New Zealand. These samples were selected to capture the onset of the cyclic glacial–interglacial sedimentation over the last 40 Myr. The drill site is located on the upper slope, 70 km east of the Waitaki river. Porewater chemistry reveals rapid sulfate consumption over the first 15 m below the seafloor (mbsf), and the presence of methane accumulation starting at 11 mbsf (Fulthorpe et al., 2011). The additional 16 samples, originally reported in Pasquier et al. (2021a), come from the offshore 1123 site. Here, the sampling strategy targeted the evolution of a sediment drift sequence to glacial–interglacial couplets over the last 40 Myr. No methane was detected along this borehole (Turchyn et al., 2006). Porewater sulfate concentrations decrease with depth, showing a concave down shape, typical of consumption by organoclastic sulfate reduction (Turchyn et al., 2006). Further details about these sequences can be found in Fulthorpe et al. (2011) and in Carter et al. (1999), respectively.

#### 2.1.2. Gulf of Lion

We report 28 newly measured samples from the European project PROMESS (PROfiles across Mediterranean Sedimentary Systems) – PRGL 1–4 (42.693°N, 3.84167°W). The drilling site is located in the Gulf of Lion (GoL), a prograding passive margin characterized by a significant subsidence rate (Rabineau et al., 2014), and high sediment inputs, mainly from the Rhône river ( $\approx 80\%$ ; Durrieu De Madron et al., 2000, Révillon et al., 2011). The water depth at the coring site (298 m) ensures continuous sedimentation under well-oxygenated conditions over the entire borehole length. Porewater chemistry was not measured during the coring campaign, yet pockmark features on the seafloor around the coring location may indicate the presence of a deep methane reservoir (Riboulot et al., 2014). Further details about this sequence can be found in Pasquier et al., 2017. Given the long residence time of sulfate in the modern ocean (i.e., 13 Myr; Kah et al., 2004), stratigraphic fluctuation in  $\delta^{34}S_{PYR}$  ( $\approx 76\%$ ) at our Gulf of Lion site have been interpreted to reflect variable degree of porewater sulfate restriction over glacial–interglacial cycles, induced by

modification of the local sedimentation rate associated with glacio-eustatic sea level variations (Pasquier et al., 2017).

#### 2.1.3. Peru margin

We report 25 samples from ODP Leg 201 – site 1229 (77.958017°S, 10.976083°E), which were previously reported in Pasquier et al. (2021b), but were not used to systematically understand the controls on Fe speciation during early diagenesis. The drilling site is located on the Peruvian continental shelf, in the Salaverry basin, within the modern oxygen minimum zone ( $\approx 150$  m water depth), where dissolved  $O_2$  concentrations in bottom waters are between 5 and 15  $\mu M$  (Scholz et al., 2017). Sediments are characterized by alternations of olive-green, well-laminated diatom ooze and a silty-clay diatom ooze with high organic matter content (Pasquier et al., 2021b). Porewater chemistry reveals sulfate consumption through the top 30 mbsf with an upper sulfate-methane transition zone (SMTZ) between 25 and 35 mbsf and a deeper SMTZ around 90 mbsf (D'Hondt et al., 2003). Dissolved sulfide was detected throughout the entire core, attesting to ongoing microbial sulfate reduction (MSR; D'Hondt et al., 2002), i.e., a microbial metabolic process during which sulfate is reduced and sulfide produced by anaerobic oxidation of organic matter (organoclastic sulfate reduction, OSR) and/or methane (AOM-SR; Jorgensen et al., 2019). Further details about this sequence can be found in D'Hondt et al. (2003).

Over the sampling interval (0–44 m), substantial variations in organic carbon deposition fluxes on the timescale of glacial–interglacial cycles have been recently interpreted to affect in-situ MSR activity and pyrite formation, resulting in the preservation of coherent stratigraphic  $\delta^{34}S_{PYR}$  variations (i.e.,  $\approx 30\%$ ; Pasquier et al., 2021b).

## 2.2. Methods

### 2.2.1. Fe speciation

Iron speciation measurements were made at the Weizmann Institute of Science using the calibrated extraction of Poulton and Canfield (2005), as modified for application to recent sediments (e.g., Goldberg et al., 2012; Matthews et al., 2017). Based on SEM observation of pseudomorphic transformation of pyrite into Fe(III) (oxyhydr)oxides, which likely resulted from post-sampling oxidation of Fe(II) phases due to storage in oxygenated conditions (Fig. S1), we adopted the extraction protocol modified by Goldberg et al. (2012), in which ferrihydrite extracted by 0.5 N HCl is considered to be an oxidation product of pyrite (discussed below). The extracted fractions are defined operationally (Henkel et al., 2016; Hepburn et al., 2020). Unsulfidized Fe phases, e.g., surface-bound Fe(II), carbonate/phosphate-associated Fe(II), and AVS were targeted first using a 0.5 N HCl extraction for 1 h at room temperature. As sulfur extractions in all four cores studied here indicated that the AVS component is negligible, we assume that no Fe(II) is associated with other Fe-sulfides and assign the  $Fe(II)_{HCl}$  pool to non-sulfidized Fe(II) minerals (i.e., mostly carbonates). Also extracted with the 0.5 N HCl extraction are some of the most reactive Fe(III) minerals such as ferrihydrite, which we termed  $Fe(III)_{HCl}$ . Due to its rapid kinetics of sulfidization (Poulton et al., 2004) and transformation to more crystalline Fe(III) (oxyhydr)oxides, it is highly unlikely that the ferrihydrite extracted by 0.5 N HCl was a part of the original sediment. Instead, we consider the  $Fe(III)_{HCl}$  fraction in these cores, which were not stored under anoxic conditions, to most likely represent the oxidation product of pyrite or other Fe(II)-bearing phases. Accordingly, the  $Fe(III)_{HCl}$  fraction was added to the chromium-reducible fraction to correct the pyrite abundance for post-sampling oxidation. More crystalline Fe(III) (oxyhydr)oxides (e.g., goethite and hematite) and mixed Fe(II)-Fe(III) (oxyhydr)oxides (e.g., magnetite) were subsequently leached using

a buffered Na-dithionite solution (termed  $\text{Fe}_{\text{di-ct}}$ ). A third extraction step targets magnetite, using Na-oxalate (termed  $\text{Fe}_{\text{oxa}}$ ). A fourth extraction step targets pyrite by reduction with chromium (termed  $\text{Fe}_{\text{CRS}}$ ). As mentioned above, we added  $\text{Fe(III)}_{\text{HCl}}$  to  $\text{Fe}_{\text{CRS}}$  to estimate the original amount of pyrite present in the cores.  $\text{Fe}_{\text{T}}$  was calculated by adding all previous extractions with Fe recovered after 1 min boiling 12 N HCl, which targets poorly reactive Fe in silicates (termed  $\text{Fe}_{\text{HCl-1min}}$ ). A comparison with a subset of 24 samples (from all boreholes except 1229) with total Fe concentration obtained by quantitative digestion yields a slope of 0.97 ( $R^2 = 0.97$ ; Fig. S2). The Fe concentration extracted by quantitative digestion was determined by inductively coupled plasma-optical emission spectrometry (ICP-OES; Ultima 2, Horiba) at the Pôle Spectrométrie Océan (PSO, UBO/CNRS/Ifremer, Brest, France).

The  $\text{Fe(II)}_{\text{HCl}}$ ,  $\text{Fe}_{\text{di-ct}}$  and  $\text{Fe}_{\text{oxa}}$  and  $\text{Fe}_{\text{CRS}}$  fractions were determined by spectrophotometry using a ferrozine assay (Stookey, 1970), 2 h after completion of the extraction. Determination of the  $\text{Fe(III)}_{\text{HCl}}$  abundance requires reduction of all  $\text{Fe(III)}$  to  $\text{Fe(II)}$ , which is achieved by reaction with ascorbic acid. The total  $\text{Fe}_{\text{HCl}}$  is then measured by spectrophotometry, and the  $\text{Fe(III)}_{\text{HCl}}$  abundance is determined by subtraction of  $\text{Fe(II)}_{\text{HCl}}$  from the total  $\text{Fe}_{\text{HCl}}$ .

As no international standards for Fe speciation were available at the time we performed the Fe sequential extractions, five samples were measured in replicate analyses in each batch to monitor precision. The replicate analyses show relative reproducibility better than 8%. Error propagation of individual steps on the calculation of the  $\text{Fe}_{\text{HR}}$  pool,  $\text{Fe}_{\text{HR}}/\text{Fe}_{\text{T}}$  and  $\text{Fe}_{\text{PYR}}/\text{Fe}_{\text{HR}}$  ratios yielded relative standard deviations better than 0.05, 0.05 and 0.02 wt%, respectively.

## 2.2.2. Pyrite sulfur content and isotopic composition

Sulfur was extracted using the chromium-reduction method (Canfield et al., 1986). This method allows recovery of all reduced sulfur present in sedimentary samples (denoted CRS and including pyrite, elemental sulfur and other Fe-sulfides phases). During extraction, approximately 2 g of bulk sample was reacted with  $\approx 25$  mL of 1 M reduced chromium chloride ( $\text{CrCl}_2$ ) solution and 25 mL of 6 N HCl for four hours just below the boiling point, in a specialized extraction line under a  $\text{N}_2$  atmosphere. The liberated hydrogen sulfide was reacted in a silver nitrate (0.1 M) trap, recovering the sulfide as  $\text{Ag}_2\text{S}$  with a reproducibility better than 5% for repeated analyses. Precipitated  $\text{Ag}_2\text{S}$  was rinsed three times using Milli-Q water, centrifuged, completely dried, and homogenized prior to analysis.

At least five bulk samples at each location and at a depth range covering the entire core were treated with 25 mL of 6 N HCl for 2 h to release acid volatile sulfur (AVS, mainly other Fe-sulfides). The  $\text{H}_2\text{S}$  liberated was then converted to  $\text{Ag}_2\text{S}$  via reaction with silver nitrate (0.1 M). None of the acid-treated samples yielded enough

$\text{Ag}_2\text{S}$  to be weighed. Following these exploratory extractions, we assume that the AVS component is negligible in our samples.

## 2.2.3. Data compilation

The dataset contains new analyses performed in this study ( $n = 54$ ) and a compilation of all published Fe speciation data available at the time of submission ( $n = 16,192$  before curation). Data were available from 61 studies of modern marine sediments (3385 samples before curation) and 171 studies of Fe speciation in sedimentary rocks (12,807 samples before curation), with ages spanning the last 2690 Myr. A full reference list is provided in the Supplementary Materials. Samples in which only some of the Fe pools were quantified, but without the full set needed to calculate both  $\text{Fe}_{\text{HR}}/\text{Fe}_{\text{T}}$  and  $\text{Fe}_{\text{PYR}}/\text{Fe}_{\text{HR}}$ , where excluded ( $n = 407$ ). We excluded cases in which  $\text{Fe}_{\text{HR}}/\text{Fe}_{\text{T}}$  and  $\text{Fe}_{\text{PYR}}/\text{Fe}_{\text{HR}}$  ratios exceed unity (622 cases). Higher than unity  $\text{Fe}_{\text{HR}}/\text{Fe}_{\text{T}}$  and/or  $\text{Fe}_{\text{PYR}}/\text{Fe}_{\text{HR}}$  may occur, for example, when  $\text{Fe}_{\text{T}}$  is measured in a separate extraction rather than as the sum of all extracted fractions or when chromium-reducible sulfur (considered to represent Fe sulfides and other reduced sulfur species) contains non-Fe sulfide minerals and organic or elemental sulfur, respectively. This left a total of 15,163 samples, almost 3 times more numerous than previous data compilations in modern marine sediments ( $n = 2990$  here compared to  $n = 1068$  in Hardisty et al., 2018) and in sedimentary rocks ( $n = 12,173$  here compared to  $n = 4300$  in Sperling et al., 2015; Hutchings and Turchyn, 2021).

The majority of samples are fine-grained clastic sediments (i.e., shale), though some are carbonate rocks (10% of the entire dataset), which were measured following recent verification of the suitability of the sequential Fe extraction protocols for carbonate rocks (Clarkson et al., 2014). A minority of the geologic samples (692) contain less than the recommended (Raiswell and Canfield, 2012; Raiswell et al., 2018) threshold of 0.5 wt% total Fe. However, when these samples were used in published studies to reconstruct past depositional environments, we included them in the compilation. A test revealed that our results are robust to the inclusion or exclusion of these Fe-poor samples (Table S1). Each sample was coded according to its age and depositional environment (i.e., inner shelf, outer shelf and basinal; see Sperling et al., 2015 for a complete description). While reported in the data compilation, we did not use the published sample's age, but all samples were binned into 16 geologic periods and/or eras according to the GSA geological timescale v.5 (Walker, 2019). The age bins are 0–2.58 Ma, 2.58–23.03 Ma, 23.03–66 Ma, 66–145 Ma, 145–201.3 Ma, 201.3–251.9 Ma, 251.9–298.9 Ma, 298.9–358.9 Ma, 358.9–419.2 Ma, 419.2–443.8 Ma, 443.8–485.4 Ma, 485.4–541 Ma, 541–1000 Ma, 1000–1600 Ma, 1600–2500 Ma and > 2500 Ma. These ages were used in the binned and statistical analyses (i.e., kernel probability density) throughout the manuscript (Tables 1–6). Additional infor-

**Table 1**

Statistical parameters of Fe speciation in modern sediments (i.e., compiled and new measurements, after curation). The first number in each table cell is the median, and the numbers in the square brackets are the [25th–75th] percentile.

Depositional environment	<i>n</i>	$\text{Fe}_{\text{T}}$ wt.%	$\text{Fe}_{\text{HR}}$ wt.%	$\text{Fe}_{\text{PYR}}$ wt.%	$\text{Fe}_{\text{HR}}/\text{Fe}_{\text{T}}$	$\text{Fe}_{\text{PYR}}/\text{Fe}_{\text{HR}}$
Open oceans ( $\geq 1000$ mbsl)	163	3.13 [2.46–3.99]	0.87 [0.58–1.20]	0.20 [0.03–0.70]	0.29 [0.21–0.41]	0.39 [0.05–0.67]
Open shelves and slopes ( $\leq 1000$ mbsl)	435	3.29 [2.79–3.94]	1.07 [0.62–1.56]	0.20 [0.12–0.38]	0.32 [0.22–0.52]	0.29 [0.10–0.49]
Interior seas	1464	3.29 [1.99–4.44]	1.22 [0.74–1.80]	0.42 [0.10–0.91]	0.40 [0.30–0.54]	0.40 [0.11–0.64]
Shore ( $\leq 15$ mbsl)	422	3.03 [2.55–4.03]	1.32 [0.80–1.88]	0.28 [0.12–0.61]	0.40 [0.31–0.55]	0.23 [0.09–0.37]
Salt Marshes	37	4.31 [3.73–4.71]	2.21 [1.82–2.58]	1.52 [0.41–1.87]	0.52 [0.42–0.72]	0.60 [0.22–0.81]
Upwelling	120	2.17 [1.65–2.94]	0.91 [0.46–1.44]	0.54 [0.18–1.07]	0.41 [0.26–0.49]	0.68 [0.40–0.81]
Hydrothermal systems	18	25.50 [10.6–32.2]	17.00 [5.8–20.8]	10.94 [0.1–14.8]	0.60 [0.41–0.72]	0.64 [0.19–0.70]
Lakes	293	4.68 [3.02–5.96]	1.58 [0.68–2.29]	0.14 [0.03–0.50]	0.37 [0.29–0.51]	0.12 [0.02–0.56]
Coral reefs and carbonate platforms	13	0.41 [0.13–0.64]	0.22 [0.09–0.23]	0.02 [0.01–0.04]	0.52 [0.39–0.67]	0.23 [0.08–0.27]
All shallow ( $\leq 1000$ mbsl)	2387	3.19 [2.16–4.47]	1.20 [0.71–1.81]	0.28 [0.09–0.68]	0.38 [0.29–0.53]	0.32 [0.09–0.56]
All	2990	3.18 [2.15–4.38]	1.17 [0.70–1.78]	0.31 [0.09–0.77]	0.38 [0.28–0.54]	0.34 [0.09–0.60]

**Table 2**

Probability of accurate reconstruction of water-column chemistry and oxidation state using  $Fe_{HR}/Fe_T$  and  $Fe_{PVR}/Fe_{HR}$ . The total number of analyses corresponding to a specific water-column chemistry and oxidation state ( $n$ , after curation) is shown in the second column. The probability and number of accurate reconstructions according to the suggested field boundaries for modern environments (Poulton and Canfield, 2011) and ancient sediments (Raiswell et al., 2018) are shown in the third and fourth columns, respectively.

Seawater chemistry and oxidation state	Accurate reconstructions [%( $n$ )]				
	$n$	Modern criteria		Ancient criteria	
		$Fe_{HR}/Fe_T = 0.38$	$Fe_{PVR}/Fe_{HR} = 0.7$	$Fe_{HR}/Fe_T = 0.22$	$Fe_{PVR}/Fe_{HR} = 0.8$
Oxic	1803	55% (987)	19% (350)		
Low $O_2$	564	45% (255)	5% (26)		
Ferruginous	95	83% (79)	100% (95)		
Euxinic	528	32% (168)	25% (132)		
All	2990	50% (1489)	20% (603)		

**Table 3**

Statistical parameters of Fe speciation in sedimentary rocks. The first number in each table cell is the median, and the numbers in the square brackets are the [25th–75th] percentile.

Sample	$n$	$Fe_{HR}/Fe_T$	$Fe_{PVR}/Fe_{HR}$
<b>Depositional environment</b>			
Shallow	1275	0.40 [0.21–0.65]	0.05 [0.00–0.56]
Shelves and slopes	6844	0.47 [0.28–0.69]	0.36 [0.02–0.69]
Basinal	4054	0.40 [0.24–0.67]	0.27 [0.03–0.65]
<b>Lithology</b>			
Siliciclastic	10,697	0.43 [0.25–0.66]	0.34 [0.03–0.69]
Carbonate	1431	0.51 [0.28–0.75]	0.03 [0.00–0.35]
Chert	45	0.73 [0.65–0.84]	0.51 [0.21–0.66]
<b>Type</b>			
Core	5115	0.44 [0.24–0.68]	0.57 [0.23–0.79]
Outcrop	7058	0.44 [0.26–0.67]	0.08 [0.00–0.50]

**Table 4**

Statistical parameters of Fe speciation in sedimentary rocks grouped by geologic era. The first number in each table cell is the median, and the numbers in the square brackets are the [25th–75th] percentile.

Geologic era	$n$	$Fe_{HR}/Fe_T$	$Fe_{PVR}/Fe_T$
Cenozoic	3298	0.41 [0.29–0.55]	0.39 [0.10–0.65]
Mesozoic	1200	0.63 [0.42–0.79]	0.41 [0.01–0.70]
Paleozoic	4638	0.47 [0.28–0.72]	0.43 [0.04–0.70]
Neoproterozoic	3095	0.38 [0.23–0.62]	0.04 [0.00–0.34]
Mesoproterozoic	1281	0.35 [0.17–0.54]	0.33 [0.05–0.76]
Paleoproterozoic	1193	0.39 [0.21–0.62]	0.31 [0.06–0.62]
Neoproterozoic	458	0.35 [0.23–0.61]	0.51 [0.28–0.81]

**Table 5**

Statistical parameters of Fe speciation in sedimentary rocks grouped by Phanerozoic geologic periods. The first number in each table cell is the median, and the numbers in the square brackets are the [25th–75th] percentile.

Phanerozoic period	$n$	$Fe_{HR}/Fe_T$	$Fe_{PVR}/Fe_T$
Quaternary	2990	0.89 [0.28–0.54]	0.34 [0.09–0.60]
Neogene	200	0.56 [0.46–0.64]	0.70 [0.52–0.82]
Paleogene	108	0.52 [0.46–0.59]	0.77 [0.72–0.80]
Cretaceous	514	0.65 [0.42–0.81]	0.58 [0.21–0.72]
Jurassic	248	0.52 [0.35–0.74]	0.61 [0.16–0.77]
Triassic	438	0.68 [0.48–0.79]	0.01 [0.00–0.30]
Permian	376	0.55 [0.40–0.71]	0.45 [0.01–0.67]
Carboniferous	143	0.73 [0.49–0.89]	0.15 [0.00–0.69]
Devonian	324	0.30 [0.21–0.70]	0.78 [0.68–0.85]
Silurian	153	0.34 [0.19–0.45]	0.48 [0.16–0.75]
Ordovician	970	0.42 [0.28–0.63]	0.58 [0.33–0.71]
Cambrian	2672	0.50 [0.28–0.75]	0.25 [0.01–0.62]

**Table 6**

Probability of accurate reconstruction of porewater chemistry and oxidation state using  $Fe_{PVR}/Fe_{HR}$ . The total number of analyses corresponding to a specific water-column chemistry and oxidation state ( $n$ , after curation) is shown in the second column. The probability and number of accurate reconstructions according to the suggested  $Fe_{PVR}/Fe_{HR}$  boundary (i.e., 0.7; Hardisty et al., 2018) is shown in the third column.

Porewater chemistry and oxidation state	Accurate reconstructions [%( $n$ )]	
	$n$	$Fe_{PVR}/Fe_{HR} = 0.7$
Fe-dominated	981	91% (893)
Sulfidic	1076	31% (341)
All	2057	45% (1234)

mation, such as the sampling strategy (i.e., core vs outcrop) and the lithology (as mentioned in the original publications), are also reported for all samples and discussed, as necessary.

Modern samples were also classified by water depth (meters below sea level, hereafter mbsl), latitude (degrees decimal minutes), longitude (degrees decimal minutes), depositional environment (open oceans (>1000 mbsl), open shelves and slopes ( $\leq 1000$  mbsl), interior seas (e.g., Black Sea, Baltic Sea or Fjords), shallow sub-wave base ( $\leq 15$  mbsl), salt marshes, upwelling zones, hydrothermal vents, coral reefs and carbonate platforms), ocean basin, seawater oxygenation state (oxic, low  $O_2$ , ferruginous, euxinic), and porewater chemistry (Fe-dominated, sulfidic). For each modern sample, the seawater chemistry was assigned according to the overlying seawater dissolved  $O_2$ ,  $H_2S$  and  $Fe^{2+}$  concentrations at the time of sampling. For long boreholes, when the seawater chemistry at the time of deposition is unknown, we assigned the seawater chemistry according to Fe speciation as reported in the original manuscript. Thus, for this subset of samples, agreement between Fe speciation-based and “true” water-column chemistry is complete. Consequently, the finding of any statistical discrepancy (at the level of the entire compilation) between true and Fe speciation-based water column chemistry is based on a conservative approach, which is to say that agreement between true and speciation-based chemistry in our analysis is probably more common than in reality. Low  $O_2$  was defined as  $<15 \mu M$  dissolved  $O_2$  but lacking detected sulfide. When possible, porewater chemistry was assigned as mentioned in the original publication. When no porewater chemistry was mentioned, we attempted to find the missing information in the available literature, yet 32% of samples ( $n = 933$ ) remained without porewater chemistry information.

### 3. Results

#### 3.1. Iron speciation in modern river sediments

The  $Fe_{HR}/Fe_T$  ratio of suspended sediments from the Waitaki River, New Zealand ( $0.30 \pm 0.01$ ,  $2\sigma$ ), measured in this study, falls within the range of previously reported river suspended sediments (Poulton and Raiswell, 2002).

#### 3.2. Iron speciation in modern marine sediments

We measured Fe speciation in 54 samples from 2 long sedimentary cores (i.e., >50 cm). These new measurements were compiled and compared with published data (2936 samples) from  $\approx 316$  cores located worldwide (Fig. S3). The complete database ( $n = 2990$ ) is available in the Supplementary Materials.

We grouped the data by the chemistry and oxidation state of the overlying water-column, by the porewater chemistry, by the parameters of the depositional environment (i.e., water depth,  $Fe_T$ , and depositional setting) and by geographic location (latitude, longitude, basin). No dependence of  $Fe_{HR}/Fe_T$  or  $Fe_{PVR}/Fe_{HR}$  on any

of the depositional or geographic parameters was observed (Figs. S4 and S5, respectively).

The values of  $Fe_{HR}/Fe_T$  in modern marine sediments vary between 0.03 and 0.99, with a median value of 0.38 and 0.29 at water depths  $\leq 1000$  m and  $>1000$  m, respectively (Table 1). Values of  $Fe_{PYR}/Fe_{HR}$  range from 0 to 0.98 with a median of 0.32 and 0.39 at water depths  $\leq 1000$  m and  $>1000$  m, respectively. The choice of 1000 m as the limit between shallow and deep depositional environments allows direct comparison with the results of Poulton and Raiswell (2002). There is no observable relationship of  $Fe_{HR}/Fe_T$  or  $Fe_{PYR}/Fe_{HR}$  with  $Fe_T$  (Figs. S4 and S5, respectively).

Many samples deposited under either oxic or anoxic conditions lead to false seawater oxygenation reconstruction, mostly in shallow depositional environments (interior seas, open shelves and slopes, and upwelling regions; Figs. S4 and S5, respectively). For example, only 52% of modern samples deposited under oxic conditions display  $Fe_{HR}/Fe_T$  values below the 0.38 threshold suggested for modern marine sediments, and only 16% display  $Fe_{HR}/Fe_T$  values below the 0.22 threshold suggested for geologic samples. The remaining 48% or 84% are characterized by  $Fe_{HR}/Fe_T$  values that incorrectly infer anoxic conditions. Similarly, 4% and 37% of samples deposited from anoxic waters display false-oxic  $Fe_{HR}/Fe_T$  values below the 0.22 and 0.38 thresholds, respectively. Similar misbehavior of  $Fe_{PYR}/Fe_{HR}$  values is observed, where only 25% of euxinic samples have ratios above the suggested 0.8 threshold (39% if the 0.7 threshold is used). In the absence of knowledge on the euxinic nature of these modern environments, the remaining 61–75% of samples would lead to an incorrect inference of oxic or ferruginous conditions (equally distributed between oxic and ferruginous using the thresholds suggested for modern sediments, and 7% oxic, 93% ferruginous using the thresholds suggested for geologic samples). False-euxinic conditions would similarly be inferred from 3% to 11% of samples from oxygenated environments (for a  $Fe_{PYR}/Fe_{HR}$  threshold of 0.7 and 0.8, respectively). Overall, the probability that an Fe speciation analysis yields a correct classification of water-column chemistry (Table 2) is 50% using the thresholds suggested for modern sediments ( $Fe_{HR}/Fe_T = 0.38$ ,  $Fe_{PYR}/Fe_{HR} = 0.7$ ) and only 20% using the thresholds suggested for geologic samples ( $Fe_{HR}/Fe_T = 0.38$ ,  $Fe_{PYR}/Fe_{HR} = 0.7$ ).

The mismatch between actual conditions and those inferred from Fe speciation is observed at all water depths (Figs. S4 and S5). The limited number of observations obtained at water depth  $> 1000$  m (only 20% of the dataset) does not allow determination of a robust depth dependence of this mismatch (Figs. S4 and S5). However, it appears that a higher proportion of false-anoxic and false-euxinic conditions are inferred in shallow-water sediments. Samples from different depths within the sediment show no statistically significant change in  $Fe_{HR}/Fe_T$  for any of the water-column oxygenation conditions (Fig. 2). An increase in  $Fe_{PYR}/Fe_{HR}$  from  $\approx 0.15$  at the top 2 cm of sediment to  $\approx 0.40$  in deeper sediments, which is observed in the overall population of samples, appears to be driven mainly by increases in  $Fe_{PYR}/Fe_{HR}$  in sediments overlain by water with  $\geq 15 \mu M O_2$ .

When  $Fe_{HR}/Fe_T$  and  $Fe_{PYR}/Fe_{HR}$  are grouped by porewater chemistry, rather than seawater chemistry, 68% of sulfidic samples plot below the threshold indicative of sulfide accumulation in porewater (i.e., 0.7; Hardisty et al., 2018). Similarly, 9% of samples deposited in Fe-dominated porewater condition display  $Fe_{PYR}/Fe_{HR}$  values above the 0.7 threshold. These large deviations show no clear dependence on geography or parameters of the depositional environment (Figs. S4 and S5, respectively). As in the case of grouping by seawater chemistry, no statistically significant change in  $Fe_{HR}/Fe_T$  is observed with depth in the sediment (Fig. 3). The increase in  $Fe_{PYR}/Fe_{HR}$  observed in the compilation of all sediments, from  $\approx 0.15$  in the top 2 cm of sediment to  $\approx 0.40$  in deeper sediments, is a frequency-weighted average of  $Fe_{PYR}/Fe_{HR}$  increases

with depth in the sediment in sub-populations with Fe-dominated ( $\approx 0.10$  to  $\approx 0.30$ ), sulfidic ( $\approx 0.45$  to  $\approx 0.75$ ) and unspecified ( $\approx 0.05$  to  $\approx 0.4$ ) porewater chemistry.

### 3.3. Iron speciation in sedimentary rocks

We compiled Fe speciation data in 7666 samples from  $>500$  locations. The newly compiled measurements were combined and compared with previously compiled datasets ( $n = 207$  and 4300; Guilbaud et al., 2015; Sperling et al., 2015 respectively), resulting in a total of 12,173 Fe speciation data. The complete database is available in the Supplementary Materials.

We grouped the data by lithology (siliciclastic, carbonate, chert), by the depositional environment (inner shelf, outer shelf and basinal), and by the sampling method (core, outcrop).

The values of  $Fe_{HR}/Fe_T$  in the geologic record vary between 0 and 0.99, with a median value of 0.46 and 0.40 for shallow and basinal environments, respectively (Table 3). Values of  $Fe_{PYR}/Fe_{HR}$  range from 0 to 0.99 with a median of 0.31 and 0.27 for shallow and basinal environments, respectively (Table 3). The classification of the depositional environments follows the strategy of Sperling et al. (2015), allowing direct comparison with their results.

The geologic era-level results are provided in Table 4. No statistically significant temporal variation in  $Fe_{HR}/Fe_T$  and  $Fe_{PYR}/Fe_{HR}$  (at the 25th–75th percentile level) is observed among eras spanning the Neoproterozoic to the Cenozoic. The geologic period-level results for the Phanerozoic Eon are provided in Table 5, and these do not show coherent secular variation either. In the absence of clear temporal trends, anomalously high and low era/period-specific distributions of  $Fe_{HR}/Fe_T$  and  $Fe_{PYR}/Fe_{HR}$  may result from a small number of sampling locations (Fig. 8) or from post-depositional alteration.

## 4. Discussion

Below, we separately discuss the distributions of  $Fe_{HR}/Fe_T$  and  $Fe_{PYR}/Fe_{HR}$  ratios in surface (depth 0–2 cm) and subsurface (depth  $> 2$  cm) sediments. We take variations in  $Fe_{HR}/Fe_T$  and  $Fe_{PYR}/Fe_{HR}$  ratios in surface sediments to represent the variability of natural sources and the earliest diagenetic reaction and mobilization of iron (Section 4.1). Variations in deeper sediments represent the effect of burial diagenesis on Fe speciation (Section 4.2).

### 4.1. Modern variability in surface sediments

In surficial sediments (depth 0–2 cm), the distributions of  $Fe_{HR}/Fe_T$  ratios in oxygenated (including low- $O_2$ ) and euxinic environments do not differ statistically (Fig. 2). Furthermore, the range of values encountered in both oxygenated and euxinic environments is similar to the  $Fe_{HR}/Fe_T$  range observed in river suspended sediments (Fig. 1; Poulton and Raiswell, 2002). A possible exception to the above is a tail towards high  $Fe_{HR}/Fe_T$  ratios observed in surface sediments from oxic environments, which may be related to redox mobilization of iron during early diagenesis, as discussed in Section 4.2. The ferruginous environments studied and included in the compilation display a narrow range of  $Fe_{HR}/Fe_T$  ratios that differs from the oxygenated and euxinic environments (Fig. 2), but the small number of ferruginous locations studied does not permit a generalization of these results.

The similarity between surface sediment  $Fe_{HR}/Fe_T$  ratios in oxygenated and euxinic environments casts doubt on the use of this ratio in sedimentary rocks to reconstruct water-column chemistry. Moreover, we find that in sediments with a low degree of pyritization, as in some of our Gulf of Lion and New Zealand shelf samples, the  $Fe_{HR}/Fe_T$  ratio of the local Fe source is preserved, persisting

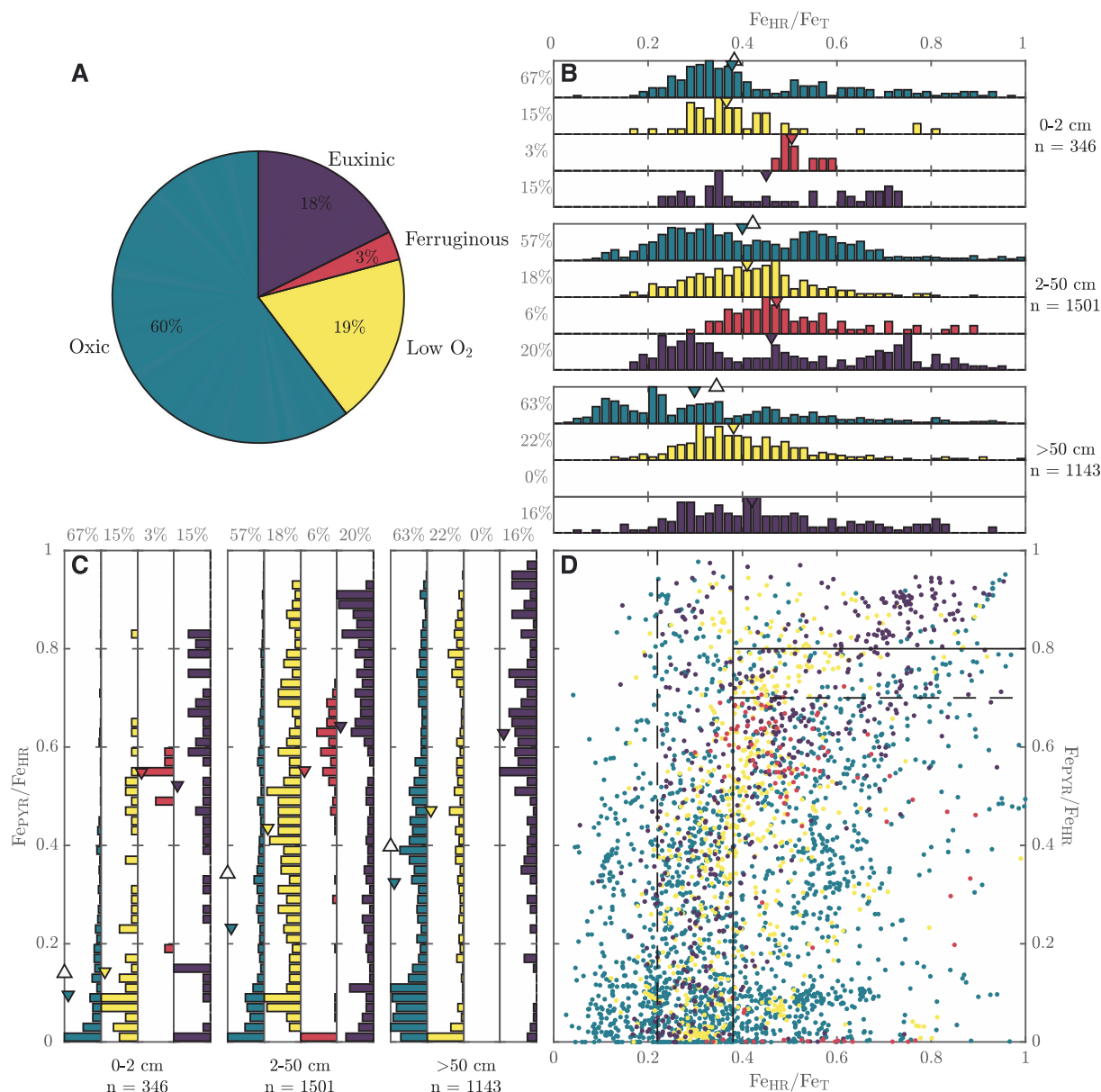


**Fig. 2.** Compiled Fe speciation data classified by seawater chemistry and oxygenation at the core location, and depth intervals within the cores. **A.** The proportion of samples underlying oxidic (green), low O<sub>2</sub> (yellow), ferruginous (red) and euxinic (purple) water columns. **B.** Distributions of Fe<sub>HR</sub>/Fe<sub>T</sub> at different depth intervals in the cores. Upward-pointing triangles show the median values for each depth interval, and downward-pointing triangles show the median values for each seawater chemistry/oxygenation state. Colors as in panel A. **C.** Distributions of Fe<sub>PYR</sub>/Fe<sub>HR</sub> at different depth intervals in the cores. Symbols and colors as in panel B. **D.** Fe<sub>HR</sub>/Fe<sub>T</sub> against Fe<sub>PYR</sub>/Fe<sub>HR</sub>. Colors as in panel A. Low oxygen is defined as <15 μM O<sub>2</sub> but lacking detectable sulfide. When available, Fe from acid-volatile sulfur extraction has been included in both the Fe<sub>PYR</sub> and Fe<sub>HR</sub> pools. Solid lines are recommended field boundaries for modern environments (Poulton and Canfield, 2011) and dashed are suggested boundaries for ancient sediments (Raiswell et al., 2018).

even in subsurface sediments that were subject to diagenesis (Fig. 4A). This suggests that Fe speciation in the local source exerts an important control on Fe<sub>HR</sub>/Fe<sub>T</sub> ratios in the sediments, but to the best of our knowledge, the Fe<sub>HR</sub>/Fe<sub>T</sub> range of the Fe source has not been considered in past reconstructions. Though deep-sea red clays ( $n = 6$ ) may display less variability (if the single datum at Fe<sub>HR</sub>/Fe<sub>T</sub> of 0.69 is considered an outlier), samples used for paleo-reconstructions are almost always obtained from shallow depositional environments (Peters and Husson, 2017).

Our results also suggest a wide range of Fe<sub>PYR</sub>/Fe<sub>HR</sub> ratios in surficial sediments, with a median (quartile) value of 0.14 (0.34) ( $n = 346$ ). Again, there are too few ferruginous data to confidently constrain the behavior of Fe<sub>PYR</sub>/Fe<sub>HR</sub> ratios in such environments. Unlike the similar Fe<sub>HR</sub>/Fe<sub>T</sub> ratios, the Fe<sub>PYR</sub>/Fe<sub>HR</sub> distribution is

wider in euxinic environments (0–0.85) than in oxygenated environments (0–~0.6), and the median value is higher (0.52 vs 0.10). However, we note that (i) 77% and 90% of Fe<sub>PYR</sub>/Fe<sub>HR</sub> ratios in the sulfidic samples are below the 0.7 and 0.8 thresholds, respectively; (ii) both the oxygenated and sulfidic samples display a wide range of Fe<sub>PYR</sub>/Fe<sub>HR</sub> ratios, so that a small number of measurements may lead to mischaracterization of the water column paleochemistry. Overall, the probability that an Fe speciation measurement yields the correct water-column chemistry is 50% and 20% with the modern and geologic thresholds, respectively (Table 2). Based on only 95 samples, the probability of an accurate ferruginous reconstruction is higher (83% and 100%, respectively), but the probability of a euxinic reconstruction is lower (32% and 25%, respectively). As discussed below, the low probability that a

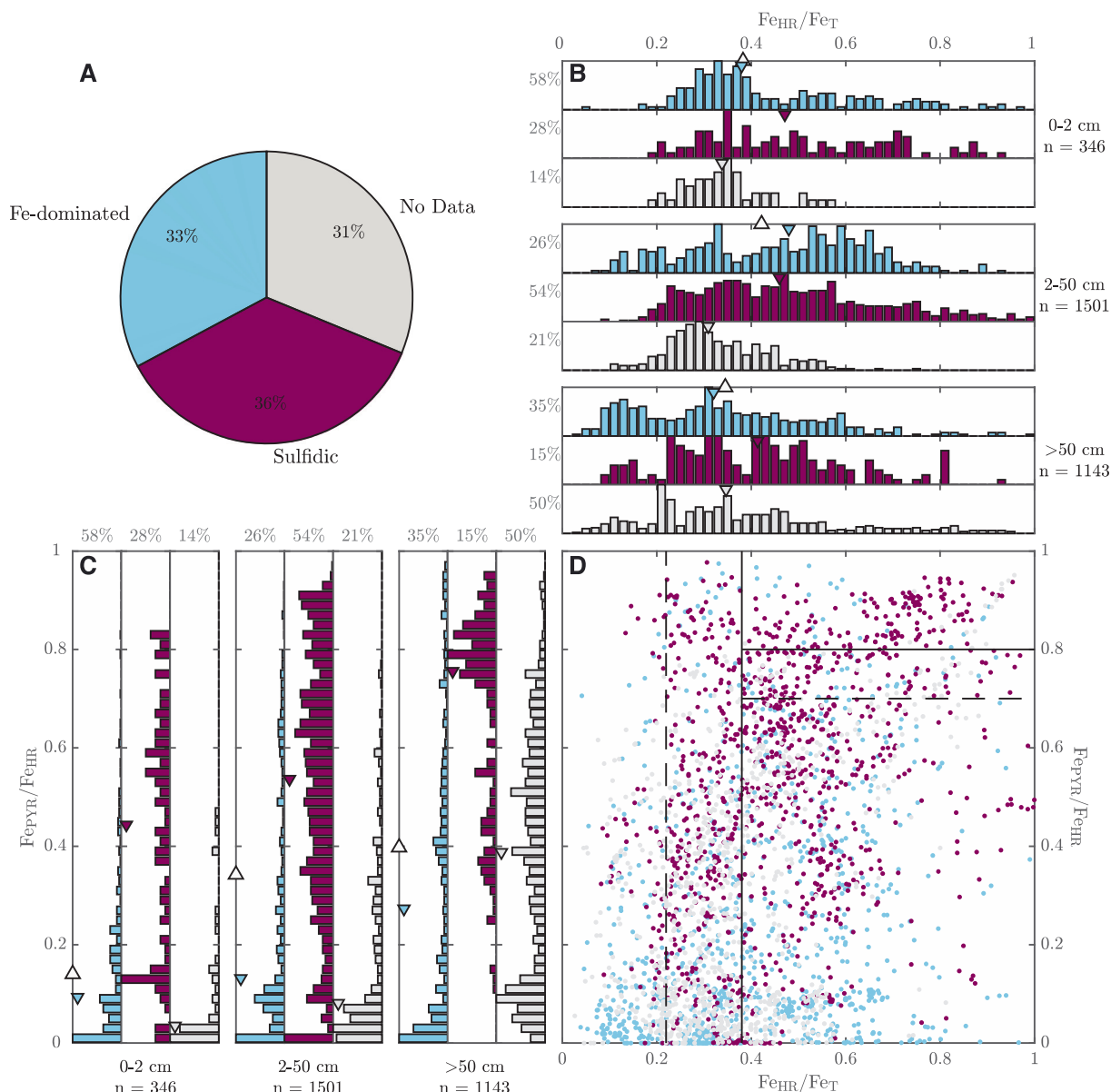


**Fig. 3.** Compiled Fe speciation data classified by porewater chemistry, and depth intervals within the cores. **A.** The proportion of samples without porewater sulfide accumulation (blue), with porewater sulfide build-up (dark purple), and from publications without porewater information (grey). **B.** Distributions of  $Fe_{HR}/Fe_T$  at different depth intervals in the cores. Triangles-up show the median values for each depth interval where triangle-down refer to the median values of each SW oxygenation state. Colors as in panel A. **C.** Distribution of  $Fe_{PYR}/Fe_{HR}$  as function of depth intervals in cores. Upward-pointing triangles show the median values for each depth interval, and downward-pointing triangles show the median values for each seawater chemistry/oxygenation state. Colors as in panel A. **D.**  $Fe_{HR}/Fe_T$  against  $Fe_{PYR}/Fe_{HR}$ . Colors as in panel A. When available, Fe from acid-volatile sulfur extraction has been included in both the  $Fe_{PYR}$  and  $Fe_{HR}$  pools. Solid lines are recommended field boundaries for modern environments (Poulton and Canfield, 2011) and dashed are suggested boundaries for ancient sediments (Raiswell et al., 2018).

euxinic reconstruction is correct may reflect the tendency of diagenetic processes in sulfate-rich environments to increase  $Fe_{PYR}/Fe_{HR}$ , thereby increasing the proportion of euxinic reconstructions. The relatively high probability of correct ferruginous reconstructions may reflect the low likelihood that diagenetic processes increase  $Fe_{HR}/Fe_T$  while decreasing (or keeping constant)  $Fe_{PYR}/Fe_{HR}$ .

We note that in all depositional environments, including those overlain by oxygenated water columns, there is appreciable pyritization in surface sediments (i.e.,  $Fe_{PYR}/Fe_{HR}$  up to  $\approx 0.2$  under oxic waters and up to  $\approx 0.5$  under low- $O_2$  waters). It is clear that this pyritization does not represent conditions in the water column or detrital pyrite, which does not survive transport and settling in an oxygenated water column (Gartman and Luther, 2014;

Johnson et al., 2014). Instead, we suggest that this pyrite is the product of earliest diagenesis and propose that higher  $Fe_{PYR}/Fe_{HR}$  ratios should be encountered in depositional environments in which diagenetic reactions dominate porewater chemistry very close to the sediment–water interface. Examples of conditions that would lead to the existence of sulfide near the sediment–water interface include high sedimentation rate and/or high organic matter content. High rates of MSR, whether in the surficial sediments themselves or at greater depth from which sulfide diffuses upwards, may lead to sufficient sulfide for pyrite generation (Liu et al., 2020; Mossmann et al., 1991; Pellerin et al., 2018). Additionally, even very close to the sediment–water interface, MSR in organic-rich niches may control the chemistry of these microenvi-

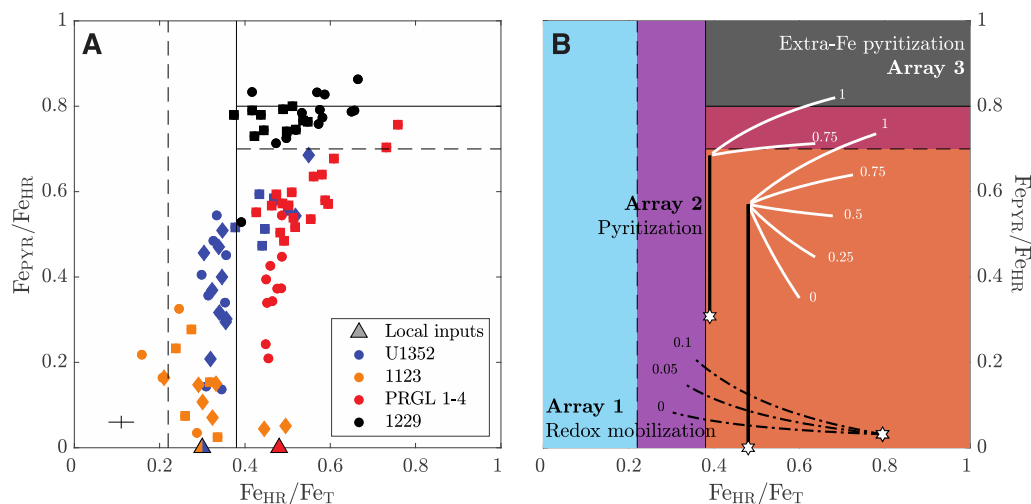


**Fig. 4.** New Fe speciation data and proposed diagenetic arrays. **A.**  $Fe_{HR}/Fe_T$  against  $Fe_{PYR}/Fe_{HR}$  in four sediment cores analyzed in this study. Solid lines are recommended field boundaries for modern environments (Poulton and Canfield, 2011) and dashed are suggested boundaries for ancient sediments (Raiswell et al., 2018).  $Fe_{HR}/Fe_T$  in local inputs is shown in upward-facing triangles. Squares, dots and diamonds represent glacial, interglacial and samples deposited prior to the onset of glacial-interglacial cycles, respectively. **B.** Schematic visualization of the 3 arrays defined in the main text. Numbers next to Array 1 indicate the proportion of  $Fe_{HR}$  lost to form  $Fe_{PYR}$ , whereas numbers next to Array 3 indicate the partitioning of the exogenous Fe between pyrite and other authigenic minerals. Coloring in these plots corresponds to the redox interpretation color scheme used throughout this manuscript (refer to Fig. 1).

ronments, making them suitable for pyrite formation, while the bulk sediment at these depths may still be oxygenated. Lastly, the availability of dissolved and particulate oxidants in surface sediments is expected to give rise to sulfur species of intermediate oxidation state (e.g., elemental sulfur, polysulfides, various sulfur oxyanions), which have been argued to increase rates of pyrite formation (Peiffer et al., 2015; Rickard, 2012a). Thus, the timescale for pyrite formation may be relatively short in surficial sediments, possibly contributing to the elevated  $Fe_{PYR}/Fe_{HR}$  ratios.

#### 4.2. Evolution of Fe speciation during early diagenesis

From the distribution of  $Fe_{HR}/Fe_T$  and  $Fe_{PYR}/Fe_{HR}$  ratios in modern marine sediments, it appears that the chemical composition and oxidation state of the water column is only rarely recorded in Fe speciation data. Once deposited, sediments are subject to a wide range of diagenetic processes, including microbially-mediated redox reactions and mineral formation reactions. Upon the exhaustion of dissolved  $O_2$ , remineralization of organic matter by anaerobes proceeds by a succession of terminal electron acceptors, the reduction of which provides progressively less energy (Bernier, 1981; Froelich et al., 1979). Of these, dissimilatory microbial reduction of Fe(III) (oxyhydr)oxides (DIR) is expected to mobilize Fe that was locked in mineral form. The dissolved Fe(II) released by these reactions is free to diffuse and react with other porewater compounds. MSR produces sulfide, which reacts with various forms of Fe, including solid Fe(III) (oxyhydr)oxides and dissolved Fe(II), to form Fe sulfide minerals. Thus, DIR and MSR affect both the transport of Fe and its reaction, thereby potentially affecting Fe speciation in the sediment.

To interpret Fe speciation data from buried sediments and sedimentary rocks it is crucial that we understand the effects of the above diagenetic processes on Fe speciation. The changes in Fe speciation expected to arise from diagenetic processes may be observed by dividing the sediments into depth bands below the sediment–water interface. The depth intervals chosen for this analysis were 0–2 cm (surficial sediments, discussed above), 2–50 cm and >50 cm. We observe no statistically significant change in  $Fe_{HR}/Fe_T$  ratios over these depth bands (Figs. 2 and 3), despite clear evidence for anaerobic remineralization of organic matter (DIR and/or

MSR) in most of the profiles included in the porewater compilation. The  $Fe_{HR}/Fe_T$  ratio over most of four profiles measured in this study closely corresponds with the  $Fe_{HR}/Fe_T$  ratio of the local Fe source (Fig. 4). We suggest that depth-invariant average  $Fe_{HR}/Fe_T$  ratios (Figs. 2 and 3) likewise reflect the local sources of Fe to the compiled sediments.

In contrast with approximately depth-invariant average  $Fe_{HR}/Fe_T$  ratios, a clear increase in  $Fe_{PYR}/Fe_{HR}$  ratios is observed with depth in the sediment, indicating diagenetic pyrite formation. The peaks of  $Fe_{PYR}/Fe_{HR}$  distributions shift to higher values and/or the distributions develop high  $Fe_{PYR}/Fe_{HR}$  tails, irrespective of water-column chemistry (Fig. 2). As expected, the trend of increasing  $Fe_{PYR}/Fe_{HR}$  ratio with depth becomes less clear when porewater chemistry is considered, with ferruginous porewater consistently displaying low  $Fe_{PYR}/Fe_{HR}$  ratios (although a slight increase is observed), and sulfidic porewater displaying higher  $Fe_{PYR}/Fe_{HR}$  ratios. In samples for which porewater chemistry was not measured ( $\approx 30\%$  of compiled modern sediments), the distribution of  $Fe_{PYR}/Fe_{HR}$  ratios remains relatively unchanged in our two upper depth bins (0.2 cm, 2–50 cm), but substantial pyritization is observed at greater depths (Fig. 3C). Of the samples deposited from an oxygenated water column that display  $Fe_{PYR}/Fe_{HR}$  ratios higher than the 0.7 threshold (i.e., false-euxinic samples), at least 67% may be explained by the existence of sulfide in the porewater (for 17% there is no information on the presence/absence of porewater sulfide). On the other hand,  $\approx 68\%$  of all samples with known porewater sulfide plot below the 0.7 threshold. That is, the Fe speciation in these samples does not reflect the chemistry of the porewater. Overall, only 45% of reconstructions accurately capture porewater chemistry and oxidation state (Table 6). As in the case of water-column chemistry and oxidation, the proportion of correct reconstructions of porewater chemistry and oxidation is high in depositional environments with  $Fe^{2+}$ -dominated porewater (91%) and low in environments with sulfidic porewater (31%).

Other than the global depth-dependent trends in  $Fe_{PYR}/Fe_{HR}$  ratios in modern marine sediments, examination of data from individual sediment cores in  $Fe_{HR}/Fe_T$ – $Fe_{PYR}/Fe_{HR}$  space reveals three types of arrays. The first of these arrays (henceforth Array 1) is evident in the shallow parts of Fe speciation depth profiles in sediments that become anoxic (Fig. S6 and Table S3). Array 1 is

characterized by an appreciable decrease in  $Fe_{HR}/Fe_T$  accompanied by variable increase in  $Fe_{PYR}/Fe_{HR}$  with depth over the first few centimeters of the sediment (Fig. 4B). We suggest that in this left-leaning trajectory,  $Fe_{HR}$  is microbially reduced but not all the released  $Fe^{2+}$  precipitates in pyrite (or AVS). Some of the  $Fe^{2+}$  diffuses upwards and is oxidized at the chemocline to form particulate Fe(III) (oxyhydr)oxides. Thus, the uppermost sediments are enriched in  $Fe_{HR}$  relative to the local input. At a steady state, the deeper sediments converge on the  $Fe_{HR}/Fe_T$  of the local sediment source, and so, the lowest  $Fe_{HR}/Fe_T$  in Array 1 is expected to most closely represent  $Fe_{HR}/Fe_T$  in the sediment source. The slope of the negative correlation in  $Fe_{HR}/Fe_T$ – $Fe_{PYR}/Fe_{HR}$  space depends on the proportion of the reduced  $Fe_{HR}$  that ends up in pyrite (or AVS). Array 1 was mostly observed in surface shelf sediments from the oxygenated parts of the Black-Sea or the Peru margin (e.g., core ID 117–120, 8 or 16–17 in the compilation; Lenstra et al., 2019; Scholz et al., 2014b; Wijsman et al., 2001, respectively). In addition, Array 1 was observed in the vicinity of hydrothermal vents in the Bransfield Strait (e.g., core ID 114; Aquilina et al., 2014) and Guyana Basin (e.g., core ID 25; Scholz et al., 2019). In these locations, the release of  $Fe^{2+}$  and its transport in bottom water (initially in dissolved form and eventually as Fe(III) (oxyhydr)oxide nanoparticles) has been shown to increase the  $Fe_{HR}/Fe_T$  ratio in the surrounding surface sediment (relative to the regional sediment source). Despite occurring under oxic water columns, by increasing surface  $Fe_{HR}/Fe_T$  ratios, redox shuttling and hydrothermal Fe inputs may lead to false ferruginous reconstructions.

The second array (henceforth Array 2) shows increasing  $Fe_{PYR}/Fe_{HR}$  by as much as 0.5–0.6, at a near-constant  $Fe_{HR}/Fe_T$  ratio, defining an approximately vertical array in  $Fe_{HR}/Fe_T$ – $Fe_{PYR}/Fe_{HR}$  space (Fig. 4B). Statistically, this trend emerges in  $\approx 60\%$  of the cores included in the modern compilation in all seawater and porewater redox conditions and give rise to increasing  $Fe_{PYR}/Fe_{HR}$  with depth in the sediment, especially in the 2–50 cm depth band (Figs. 5 and 6, Table S3). In line with previous observations, the most likely mechanism behind this vertical array is progressive pyritization in the MSR zone, where the most highly reactive Fe minerals, for example, ferrihydrite and hematite, rapidly react with porewater sulfide to form pyrite (Bernier, 1984; Canfield et al., 1992; Poulton et al., 2004). Sulfide production and pyritization may extend down to the zone of AOM-SR (e.g., Dale et al., 2009; Egger et al., 2016; Jørgensen et al., 2019; Peketi et al., 2012). Support for progressive pyritization of Fe (oxyhydr)oxides comes from the correlation between  $Fe_{PYR}/Fe_{HR}$  and the sulfur isotopic composition of pyrite ( $\delta^{34}S_{PYR}$ ) observed in the Gulf of Lion, New-Zealand, and Peru cores (Fig. 7A). In these and other sediments, drawdown and isotopic (Rayleigh-type) distillation of porewater sulfate by MSR enriches the residual sulfate in  $^{34}S$  (Fernandes et al., 2020; Liu et al., 2020; Pellerin et al., 2018; Raven et al., 2016). Porewater sulfate  $\delta^{34}S$  values increase with depth in the sediment, as do those of the sulfide product of MSR and pyrite formed from it (see Fike et al., 2015). Although  $\delta^{34}S_{PYR}$  also reflects depositional conditions and sedimentary sulfur cycling over the period of pyrite formation (e.g., Liu et al., 2020; Pasquier et al., 2021a; Pasquier et al., 2021b), in the majority of cases  $\delta^{34}S_{PYR}$  also increases with depth in the sediment. Thus, with increasing degree of pyritization (i.e.,  $Fe_{PYR}/Fe_{HR}$ ), it is expected that  $\delta^{34}S_{PYR}$  values increase, as observed (Fig. 7A).

We note that in anoxic environments the overall increase in  $Fe_{PYR}/Fe_{HR}$  observed in the sediment may be smaller due to pyrite formation in the water column (Li et al., 2011; Wilkin et al., 1996). In such cases, the  $Fe_{PYR}/Fe_{HR}$  ratio is already high (0.7–0.8) at the sediment–water interface (e.g., core ID 4 and 129 in the compilation; Pasquier et al., 2021b; Wijsman et al., 2001, respectively) and it increases by a smaller amount in the sediment (i.e., Array 2 is shorter). Where covariation of  $Fe_{HR}/Fe_T$  and  $Fe_{PYR}/Fe_{HR}$  along Array 1 is not observed, the  $Fe_{HR}/Fe_T$  value of the vertical Array 2

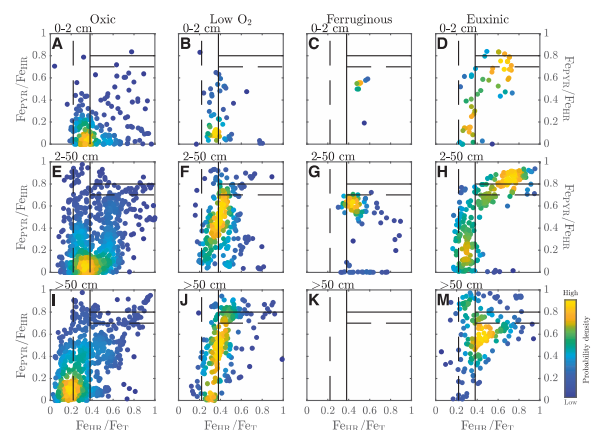


**Fig. 5.** Probability density of Fe speciation data as a function of seawater chemistry and oxidation (columns), and depth within the sediment (rows). Low O<sub>2</sub> is defined as <15  $\mu\text{M}$  dissolved O<sub>2</sub> but lacking detectable sulfide. When available, Fe from acid-volatile sulfur extraction is included in both the  $Fe_{PYR}$  and  $Fe_{HR}$  pools. Solid lines are recommended field boundaries for modern environments (Poulton and Canfield, 2011) and dashed are suggested boundaries for ancient sediments (Raiswell et al., 2018).

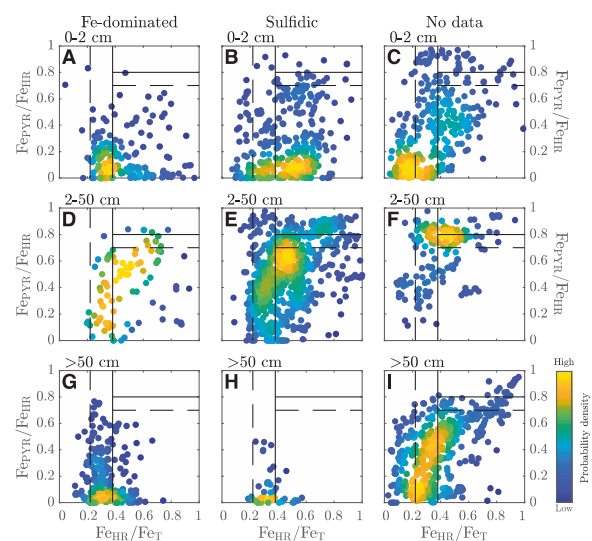


**Fig. 6.** Probability density of Fe speciation data as a function of porewater chemistry (columns), and depth within the sediment (rows). Definitions and fields are as in Fig. 5.

is expected to reflect the local Fe source. For example, Array 2 in the Gulf of Lion and New-Zealand cores starts at the  $Fe_{HR}/Fe_T$  of sediments suspended in the Rhone and Waitaki Rivers, respectively (Fig. 4A). Where both Arrays 1 and 2 are observed, mass balance requires that their intersection is at the  $Fe_{HR}/Fe_T$  of the local inputs, as argued above for the lowest  $Fe_{HR}/Fe_T$  value on Array 1. Thus, the approximately constant  $Fe_{HR}/Fe_T$  in Array 2 may generally be taken to represent the sediment source. This implies that locally high  $Fe_{HR}/Fe_T$  in sediment inputs (i.e., >0.38) and progressive pyritization will shift sediments into the ferruginous field, possibly leading to false-ferruginous reconstructions, as observed in the Gulf of Lion.

The third array (henceforth Array 3) intercepts Array 2 at high  $Fe_{PYR}/Fe_{HR}$  ratios and displays concurrent increases in  $Fe_{HR}/Fe_T$  and  $Fe_{PYR}/Fe_{HR}$  along trajectories with variable slope (Fig. 4B). The increase in  $Fe_{HR}/Fe_T$  requires addition of  $Fe_{HR}$  or transformation of some of the poorly reactive Fe to  $Fe_{HR}$ . The apparent gain of  $Fe_{HR}$  is observed in  $\approx 30\%$  of the cores included in the modern

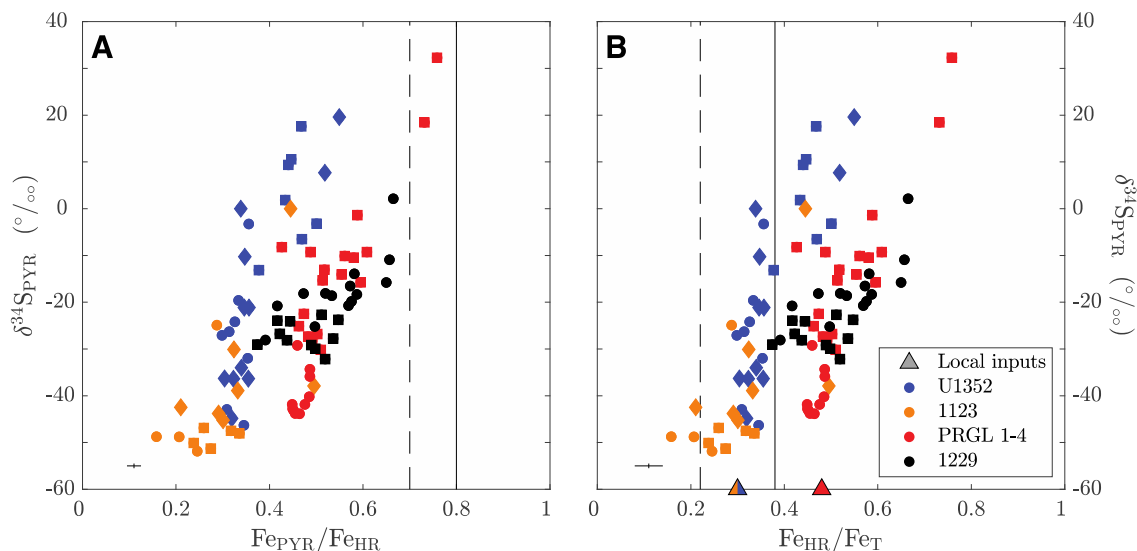


**Fig. 7.** Covariation of new Fe speciation data with  $\delta^{34}\text{S}_{\text{PYR}}$ . **A.**  $\text{Fe}_{\text{PYR}}/\text{Fe}_{\text{HR}}$  against  $\delta^{34}\text{S}_{\text{PYR}}$ . **B.**  $\text{Fe}_{\text{HR}}/\text{Fe}_{\text{T}}$  against  $\delta^{34}\text{S}_{\text{PYR}}$ . When available, Fe from acid-volatile sulfur extraction is included in both the  $\text{Fe}_{\text{PYR}}$  and  $\text{Fe}_{\text{HR}}$  pools. Solid lines are recommended field boundaries for modern environments (Poulton and Canfield, 2011) and dashed are suggested boundaries for ancient sediments (Raiswell et al., 2018).

compilation (Table S3), mostly in those in which sulfide accumulates in the porewater (Fig. 6). In such sediments, sulfide accumulates as its production rates locally exceed its removal by reaction with dissolved  $\text{Fe}^{2+}$ , Fe-bearing minerals or organic matter. It is possible that prolonged exposure of less reactive Fe-bearing minerals, such as Fe silicates, to pooled sulfide is the reason for the apparent  $\text{Fe}_{\text{HR}}$  gain (e.g., Eroglu et al., 2021). However, we note that the kinetics of these microbially mediated and abiotic reactions are slow, with half-lives  $> 1 \times 10^6$  years (Aeppli et al., 2022; Canfield et al., 1992; Poulton et al., 2004; Rickard, 2012b), which is several orders of magnitude longer than the time elapsed since the deposition of most cores included in the data-compilation. Thus, the  $\text{Fe}_{\text{HR}}$  is gained either by another mechanism, possibly exogenous, as discussed below, or by reaction with sulfide of Fe-bearing minerals that are thought to react slowly with sulfide (e.g., siderite and various silicate minerals; Canfield et al., 1992; Raiswell and Canfield, 1998). The ratio of  $\text{Fe}_{\text{T}}/\text{Al}$  may serve to distinguish between an exogenous origin and sulfidization of progressively less reactive Fe-bearing minerals as the source of the extra Fe in Array 3 (e.g., core ID 306 in the compilation; Eroglu et al., 2021). The  $\text{Fe}_{\text{T}}/\text{Al}$  ratio is expected to increase together with  $\text{Fe}_{\text{HR}}/\text{Fe}_{\text{T}}$  and  $\text{Fe}_{\text{PYR}}/\text{Fe}_{\text{HR}}$  in the former case, but not in the latter.

As an alternative to gradual reaction of less reactive Fe-bearing minerals, the additional  $\text{Fe}_{\text{HR}}$  required for Array 3 may originate outside the studied sediments. For example, resuspended Fe (oxyhydr)oxides from sites with oxygenated bottom water could be transported to sites with sulfide at or close to the SWI. The subsequent pyritization of this exogenous Fe would lead to concurrent increases in  $\text{Fe}_{\text{HR}}/\text{Fe}_{\text{T}}$  and  $\text{Fe}_{\text{PYR}}/\text{Fe}_{\text{HR}}$  (e.g., core ID 125, 132–133, 119 in the compilation; Kraal et al., 2017; Kraal et al., 2019; Lenstra et al., 2019, respectively). If the exogenous Fe were delivered at a constant rate, the result would just be an Array 2 with a higher  $\text{Fe}_{\text{HR}}/\text{Fe}_{\text{T}}$  origin than that of the local sediment input. However, temporal variations in the rate of  $\text{Fe}_{\text{HR}}$  addition are expected to lead to covariation between  $\text{Fe}_{\text{HR}}/\text{Fe}_{\text{T}}$  and  $\text{Fe}_{\text{PYR}}/\text{Fe}_{\text{HR}}$ , as observed in Array 3.

An additional source of exogenous Fe may be related to the effects of methane production and consumption on Fe(III)-bearing minerals that are otherwise bio-unavailable or slow to react with aqueous sulfide (e.g., Beal et al., 2009; Egger et al., 2015b; Jiang et al., 2013; Kato et al., 2012; Noröi et al., 2013; Sivan et al., 2011; Sivan et al., 2014; Sivan et al., 2016; Zhuang

et al., 2015). In this case, Array 3 is expected to occur deeper in the sediments (e.g., Figs. 5 and 6), as dissolved  $\text{Fe}^{2+}$  released in the methanic zone diffuses upwards to the SMTZ, where it reacts with sulfide to produce pyrite, thereby elevating both  $\text{Fe}_{\text{HR}}/\text{Fe}_{\text{T}}$  and  $\text{Fe}_{\text{PYR}}/\text{Fe}_{\text{HR}}$ . Migration of the SMTZ could lead to variable degrees of Fe enrichment, giving rise to covarying  $\text{Fe}_{\text{HR}}/\text{Fe}_{\text{T}}$  and  $\text{Fe}_{\text{PYR}}/\text{Fe}_{\text{HR}}$  (i.e., Array 3). The GoL and NZ shelf cores may be examples in which methane-related processes explain the observed Fe sulfide enrichment (i.e., an Array 3 with a slope  $\approx 1$ ), driving the  $\text{Fe}_{\text{HR}}/\text{Fe}_{\text{T}}$  ratio above the local sediment inputs concurrently with an increase in  $\delta^{34}\text{S}_{\text{PYR}}$  associated with the consumption and isotopic distillation of sulfate at/near the SMTZ (Fig. 7A). Indeed, during glacial times, local modifications of the depositional environments (i.e., higher sedimentation rate, including organic matter and Fe (oxyhydr)oxides) induced by low sea level, resulted in higher rates of OSR and AOM-SR, which likely led to episodic upward migration of the SMTZ (Pasquier et al., 2021a, 2017). At the Peru margin, similar migration of the SMTZ may be linked to local variations in the organic depositional flux rather than changes in sedimentation rate (Contreras et al., 2013; Pasquier et al., 2021b). In all cases, rapid upward displacement of the SMTZ reduces the exposure time of lithogenic Fe (oxyhydr)oxides to dissolved sulfide, possibly allowing a greater proportion to be preserved below the newly established SMTZ, and facilitating  $\text{Fe}^{2+}$  release via Fe(III)-driven AOM.

Irrespective of the source of additional  $\text{Fe}_{\text{HR}}$ , the slope of Array 3 should be governed by the partitioning of the added  $\text{Fe}_{\text{HR}}$  between pyrite and other authigenic Fe-bearing minerals (Fig. 4B). Such minerals include Fe(II)-rich carbonates or the Fe(II) phosphate vivianite, among others (Dijkstra et al., 2016; Egger et al., 2015b; Kubeneck et al., 2021). The apparent  $\text{Fe}_{\text{HR}}$  gain mostly in cores with sulfidic porewater may explain the predominantly positive slopes of Array 3 in modern sediments (Figs. 6 and S5), which suggest that the majority of added  $\text{Fe}_{\text{HR}}$  is sequestered in pyrite and not in other Fe-bearing diagenetic products. Again, irrespective of the source of additional  $\text{Fe}_{\text{HR}}$ , and depending on the  $\text{Fe}_{\text{HR}}/\text{Fe}_{\text{T}}$  ratio of local sediment inputs, the processes described above, which give rise to concurrent increases in  $\text{Fe}_{\text{HR}}/\text{Fe}_{\text{T}}$  and  $\text{Fe}_{\text{PYR}}/\text{Fe}_{\text{HR}}$ , may lead to false-ferruginous or false-euxinic reconstructions.

Importantly, we note that the existence of any of the arrays described above in sedimentary sequences does not necessarily imply an evolution with burial depth and/or time (see Fig. S7).

Although burial depth trends in Fe speciation often display the patterns described above (e.g., early increase in  $\text{Fe}_{\text{PYR}}/\text{Fe}_{\text{HR}}$  as in Array 2, followed by coupled increase in  $\text{Fe}_{\text{HR}}/\text{Fe}_{\text{T}}$  and  $\text{Fe}_{\text{PYR}}/\text{Fe}_{\text{HR}}$  as in Array 3; Fig. S5), such arrays could also represent a variable degree of diagenetic evolution from the same starting conditions (i.e., from the same local inputs at the sediment–water interface). The GoL and NZ cores provide examples, in which glacial samples (squares in Fig. 4) cluster at relatively high  $\text{Fe}_{\text{HR}}/\text{Fe}_{\text{T}}$  and  $\text{Fe}_{\text{PYR}}/\text{Fe}_{\text{HR}}$ , interglacial samples (dots in Fig. 4) have relatively low  $\text{Fe}_{\text{HR}}/\text{Fe}_{\text{T}}$  and  $\text{Fe}_{\text{PYR}}/\text{Fe}_{\text{HR}}$ , and the space between these extremes is populated by samples depending on the degree of glaciation. In these cases, Arrays 2 and 3 reflect changing diagenetic regimes rather than evolution with depth in the sediment (Fig. S7). Since Arrays 1, 2 and 3 are statistically observed irrespective of classification by seawater redox, porewater chemistry or depth intervals (Table S3), we suggest that the existence of these arrays in sedimentary rocks may be used to make inferences about past diagenetic processes (i.e., redox surface mobilization, pyritization and extra-Fe pyritization). For example, we found that  $\approx 21\%$  of boreholes/outcrops included in our geologic compilation show the existence of Array 2-type evolution, and  $\approx 18\%$  show Array 3-type evolution (Table S4). These percentages should be considered underestimates, because a significant number of boreholes/outcrops do not contain enough data to confidently identify the arrays (i.e., 13–26% of boreholes/outcrops are characterized by <5–10 Fe speciation data), and others may have suffered from late-stage pyrite oxidation (see Section 4.3). Hence, with sufficient sampling frequency, and accounting for post-depositional oxidation, we suggest that Fe speciation in about half of the sections in the sedimentary rock record could be used to constrain diagenetic processes. It is less clear that these same proxies inform the water-column chemistry or oxidation state.

#### 4.3. Implications for Fe speciation-based reconstructions of seawater chemistry

In addition to investigating the controls on Fe speciation trends in modern marine sediments, we compiled previously published geologic Fe speciation data (Figs. 8 and 9). Below we discuss observations based on this compilation, including sampling biases, long-term trends, and possibly incorrect seawater chemistry and oxidation state reconstructions.

About 50% and 22% of all Fe speciation analyses come from Precambrian and early Paleozoic units, respectively. The time spanning the Mesoproterozoic to the end Cambrian, which saw substantial geochemical shifts and biological innovations, hosts approximately 58% of all analyses. Though this temporal sampling bias results in uncertainty on trends observed in the compiled data, only 3 time bins contain <200 samples; these are the Paleogene, Carboniferous and Silurian with 108, 143 and 153 samples, respectively (Table 5).

Within uncertainty, no clear secular trend in  $\text{Fe}_{\text{HR}}/\text{Fe}_{\text{T}}$  is observed over the past  $\approx 2,500$  million years (Fig. 8), despite radical changes to the chemistry of the oceans and atmosphere over this time interval. Similarly, no clear secular trend is observed in  $\text{Fe}_{\text{PYR}}/\text{Fe}_{\text{HR}}$  (Fig. 8). A possible exception to the above is the occurrence of elevated  $\text{Fe}_{\text{PYR}}/\text{Fe}_{\text{HR}}$  values in the late Paleozoic and in the Mesozoic, though it is unclear that changes in seawater chemistry are the causes for this change, as discussed below. The absence of meaningful trends over the last  $\approx 2,500$  Myr (i.e., a period over which the increase in the oxidation state of Earth's atmosphere and oceans is well documented; e.g., Cole et al., 2016; Farquhar et al., 2000; Hardisty et al., 2014; Partin et al., 2013; Stolper and Keller, 2018) reinforces the notion, based on our analysis of modern marine sediments, that Fe speciation data do not constrain

water-column chemistry, reflecting instead the local sediment source and diagenetic processes.

A close examination of the last 200 Myr of the geologic compilation, excluding extensively sampled Quaternary marine sediments, reveals that  $\approx 75\%$  of the available data originate from the so-called Ocean Anoxic Events (OAEs). During these events, high concentrations of organic carbon in sedimentary rocks accompanied by shifts in Fe speciation have been interpreted to reflect episodes in which parts of the ocean became temporarily anoxic, in response to global changes in climate, solid-Earth emissions or biogeochemical cycles (e.g., Jenkyns, 2010). However, as sedimentary organic carbon is the main driver of metabolic activity during burial, including MSR, any increase in its concentration and/or reactivity is expected to exert a strong local control on the preserved Fe mineralogy (e.g., Pasquier et al., 2021b), and thus may have led to false-anoxic reconstructions. For example during the Cenomanian-Turonian OAE event, stratigraphic variations and/or compiled datasets show clear evidence of a diagenetic influence on Fe speciation (i.e., Arrays 2 or 3; Fig. S8), suggesting that false-anoxic reconstructions are possible.

Irrespective of Fe speciation-based reconstructions of seawater chemistry during the OAEs, the dominance of OAEs in the Fe speciation data ( $\approx 75\%$ ) is contrasted by both their relative infrequency (9 occurrences) and their short duration (<100 kyr; Jenkyns, 2000), which means that they collectively represent only  $\approx 0.5\%$  of the last 200 Myr. The OAEs serve to demonstrate that interesting episodes in Earth history are preferentially sampled, irrespective of how well they represent the long-term properties of the Earth system. Like OAEs, times of mass extinction are likely overrepresented in Phanerozoic datasets, and in some cases, a connection between periods of reconstructed anoxia and mass extinctions has been proposed (e.g., Bond and Grasby, 2017). However, many of these cases are in fact associated with periods of sea-level fall, which have been shown to affect the local diagenetic regime through changes in sedimentation rate (Pasquier et al., 2017, 2021a), as in the GoL and NZ sediments studied here. The sampling biases described above suggest that the accepted history of seawater chemistry and oxidation state may rely too heavily on time intervals that are not representative of long-term average conditions. The kernel density plots of Fe speciation data binned according to geologic era and period may support this notion, as the Archean and Proterozoic time bins preserve apparently more oxic conditions than Paleozoic and Mesozoic time bins (Fig. 9), despite an established increase in the oxidation state of Earth's atmosphere and oceans over time (Cole et al., 2016; Farquhar et al., 2000; Hardisty et al., 2014; Partin et al., 2013; Stolper and Keller, 2018).

In addition to unrepresentative sampling of depositional environments and time intervals that record the long-term average conditions in the ocean, we suggest that sampling artefacts and post-depositional processes further influence Fe speciation-based reconstructions. Raiswell et al. (2018) provided several crucial guidelines for assessment of the fidelity of Fe speciation data, including (i) selection of “fresh un-weathered” material, (ii) exclusion of samples subjected to extensive alteration by metamorphism or interaction with post-depositional fluids, and (iii) rejection of samples with low  $\text{Fe}_{\text{T}}$  and/or low TOC. The first two criteria are qualitative, providing some freedom in sample inclusion. In many cases the TOC concentrations are not released together with the Fe speciation data, making it difficult to evaluate compliance with this aspect of the third criterion. The  $\text{Fe}_{\text{T}}$  threshold for reliable reconstructions has been recommended as 0.5 wt% (Raiswell and Canfield, 2012; Raiswell et al., 2018), though we have shown that samples with  $\text{Fe}_{\text{T}}$  at and above this threshold often yield Fe speciation-based classifications that do not agree with the actual water-column chemistry. Overall, we found that only a few percent of all studies in which Fe speciation data are presented

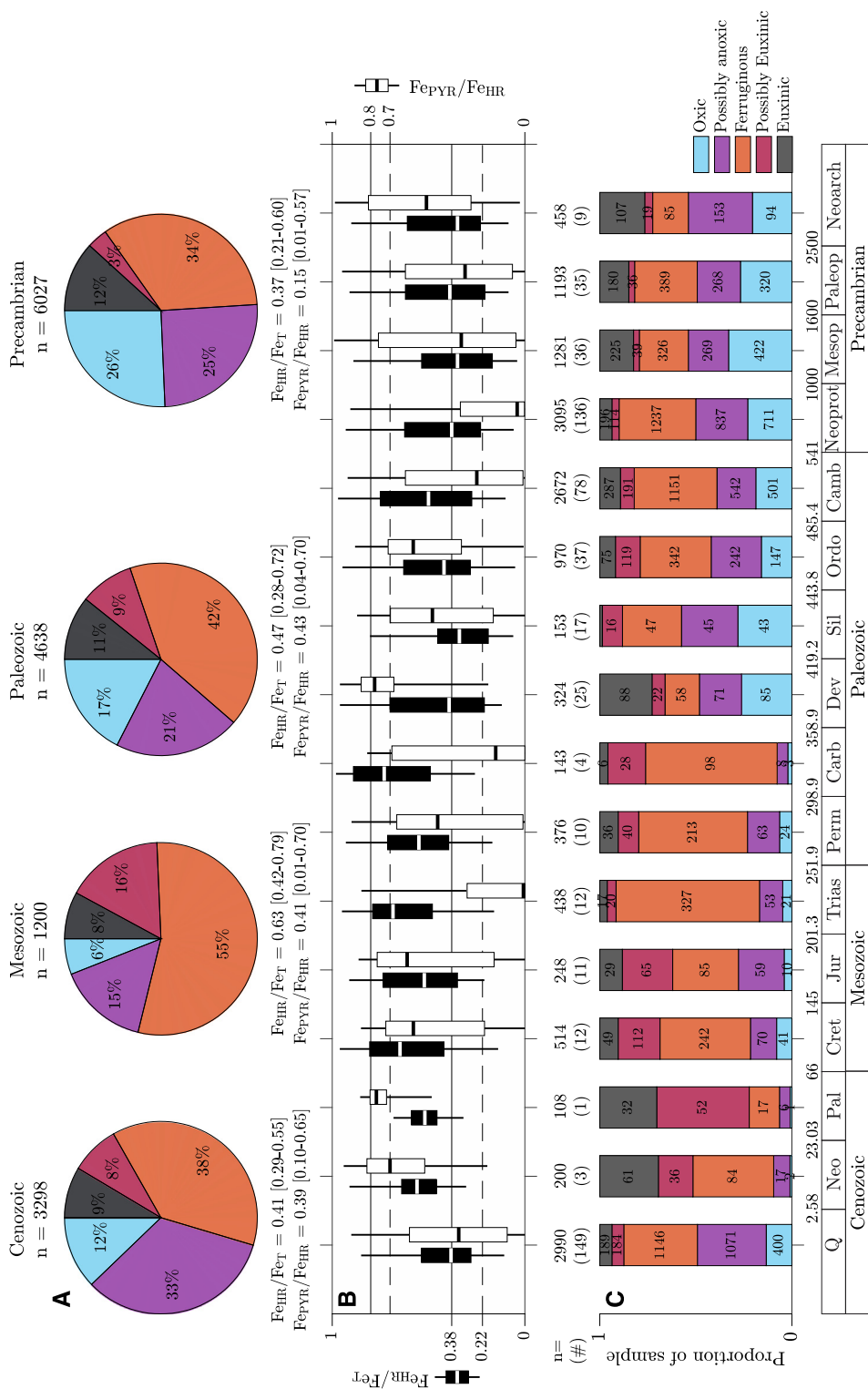


**Fig. 8.** Compiled Fe speciation data in modern sediments and sedimentary rocks. **A.** The proportion of samples indicating oxic (blue), possibly anoxic (purple), ferruginous (orange), possibly euxinic (red), and euxinic (black) conditions using the existing Fe speciation interpretive framework, binned by geologic era/eon. Numbers within charts indicate the proportion of samples. Era/eon median and 25th to 75th percentiles (in square brackets), and the total sample number are shown below and above the pie charts, respectively. **B.** Box and whisker plots for Fe<sub>HR</sub>/Fe<sub>T</sub> (black boxes) and Fe<sub>PYR</sub>/Fe<sub>HR</sub> (white boxes) binned by geologic period. Dashed horizontal lines show the recommended field boundaries in the modern ocean and solid lines show suggested boundaries for ancient sediments and sedimentary rocks. **C.** Stacked proportions of samples indicating oxic, possibly anoxic, ferruginous, possibly euxinic, and euxinic conditions, using the existing interpretive framework and binned by geologic period. Bin age boundaries are indicated on top of the geologic timeline according to the GSA geologic time scale v.5 (Walker et al., 2018). Colors are as in panel A. Total sample numbers and the number of sampled locations (in parentheses) are shown above the column charts.

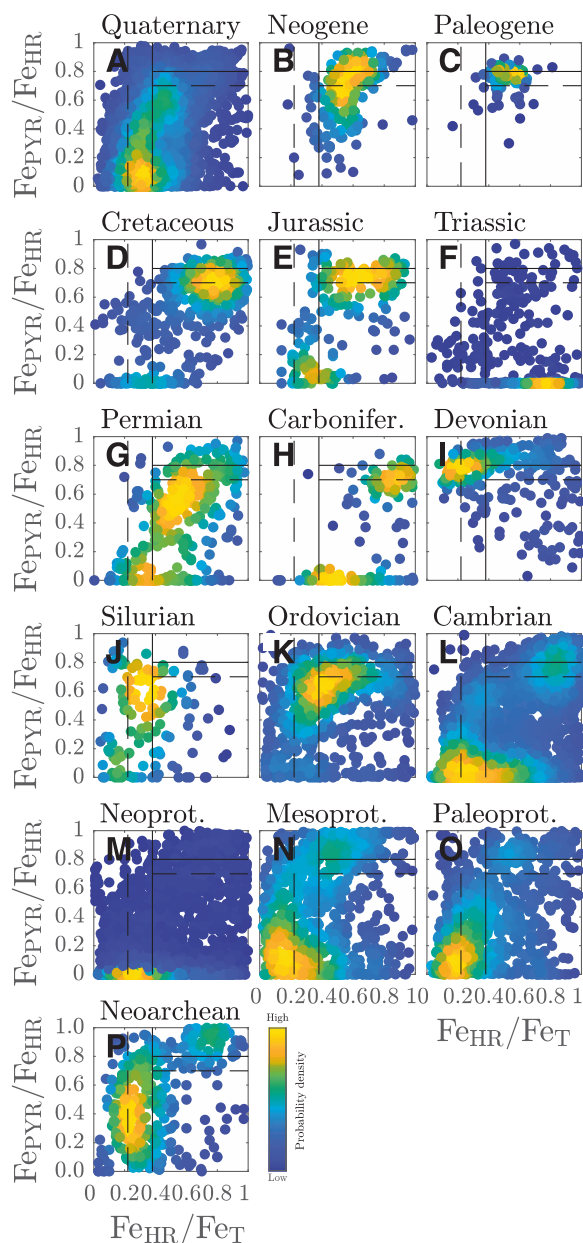


**Fig. 9.** Probability density of Fe speciation data as a function of geologic periods (i.e., Quaternary to Cambrian) and eras (i.e., Neoproterozoic to Neoproterozoic). Solid lines are recommended field boundaries for modern environments (Poulton and Canfield, 2011) and dashed are suggested boundaries for ancient sediments (Raiswell et al., 2018).

reported compliance with all three screening requirements. A higher threshold of 5 wt% has been suggested, to avoid diagenetic overprinting by sulfidization (Hutchings and Turchyn, 2021), and naturally, even a smaller percentage of studies would comply with such a threshold.

Despite reported efforts to avoid weathered surfaces in most Fe speciation studies, there is a marked difference in  $Fe_{PYR}/Fe_{HR}$  (but not in  $Fe_{HR}/Fe_T$ ) between drill-core and outcrop samples (Fig. S9; e.g., Ahm et al., 2017), with outcrop samples tending towards lower  $Fe_{PYR}/Fe_{HR}$ . Though it is possible that pyrite-rich rocks are less frequently sampled in outcrop due to an expectation of poor preservation, we suggest that lower  $Fe_{PYR}/Fe_{HR}$  in outcrop samples is most readily explained by a greater degree of oxidative alteration of outcrop samples than drill-core samples. Under today's

oxygenated atmosphere, pyrite and FeS readily oxidize in most rocks, even away from outcrop faces, at depth in unexposed units, and in units with poor hydraulic connectivity (Gu et al., 2020a, 2020b; Kemeny et al., 2021a, 2021b; Wan et al., 2019). A decrease in  $Fe_{PYR}/Fe_{HR}$  concomitant with no change in  $Fe_{HR}/Fe_T$  is naturally explained by oxidation of pyrite to form Fe(III) (oxyhydr)oxides, potentially leading to false-ferruginous reconstructions. Perhaps most clearly, we consider the presence of ferrihydrite, which rapidly reacts with dissolved sulfide (Canfield et al., 1992; Poulton et al., 2004) or transforms to more crystalline (oxyhydr)oxides (e.g., goethite), as a strong indication for late-stage oxidation of Fe(II)-bearing minerals, notably FeS and pyrite. Hence, we suggest that any Fe recovered by selective leaching of ferrihydrite (Henkel et al., 2018; Henkel et al., 2016; Hepburn et al., 2020) should be considered as part of the  $Fe_{PYR}$  pool. We note that pyrite and FeS oxidation is not limited to the field and may occur during sample storage unless efforts are made to exclude  $O_2$ .

Avoidance of oxidatively altered samples may be achieved by systematic use of detailed petrographic analyses and/or X-ray elemental mapping (SEM-EDS). Prior to crushing or chemical extraction of Fe (or other wet-chemical protocols), such analyses should be able to reveal pyrite cores surrounded by rims of Fe (III) (oxyhydr)oxides at the grain scale (i.e., approximately 5  $\mu m$ ; see examples in Gu et al., 2020a; Mahoney et al., 2019 among others). Additionally, measurements of S speciation and isotopic composition could valuably inform the pre-alteration Fe speciation. For example, low  $\delta^{34}S$  values of soluble sulfate typically indicate an origin from oxidation of sulfide minerals or organic S, especially if carbonate-associated sulfate displays higher  $\delta^{34}S$  values (e.g., Bowman et al., 2021; Shawar et al., 2018; Wotte and Strauss, 2015). Quantifying the amount of such soluble sulfate, for example using coupled Fe-S speciation and S isotopes, provides a lower limit on the amount of late-stage (in-situ or during handling and/or storage) FeS and pyrite oxidation, as some of the sulfate produced is likely to have remained in solution and mobilized.

Lastly, because Fe is mobile during sub-greenschist or higher-grade metamorphism (see Slotznick et al., 2018a), geologic Fe speciation data may be further compromised by metamorphic processes. For example, formation of pyrrhotite from Fe-bearing carbonate is well documented, even at relatively low burial temperature (i.e.,  $\approx 75$ – $100$  °C; e.g., Asael et al., 2013; Bosco-Santos et al., 2020; Doyle et al., 2018; Gilleaudeau and Kah, 2015; Nguyen et al., 2019; Partin et al., 2015; Poulton et al., 2010; Reinhard et al., 2013; Reuschel et al., 2012; Slotznick et al., 2018a). As pyrrhotite is extracted together with pyrite during the chromium reduction step, and this may lead to spuriously high  $Fe_{PYR}/Fe_{HR}$ . Metamorphic formation of Fe-bearing silicates, such as garnet and amphibole, may additionally depress  $Fe_{HR}/Fe_T$  (Slotznick et al., 2018a). Careful petrographic study to identify the presence and history of pyrrhotite and Fe-bearing carbonates and silicates is thus crucial for accurate reconstructions of the original Fe speciation in metamorphosed rocks. If such measures are not taken, samples containing pyrrhotite and/or those with a complex metamorphic history should be avoided.

In summary, our compiled Fe speciation data do not show statistically significant secular trends in either  $Fe_{HR}/Fe_T$  or  $Fe_{PYR}/Fe_{HR}$ , despite the presence of independent indications for changes in the oxidation state of Earth's oceans and atmosphere (e.g., Cole et al., 2016; Farquhar et al., 2000; Hardisty et al., 2014; Partin et al., 2013; Stolper and Keller, 2018). We suggest that this reflects sampling biases and diagenetic alteration, despite best practices aimed at minimizing the effects of post-depositional alteration on Fe speciation data, as discussed above. As such, it may be necessary to revisit many of the paleo-environmental inferences based on sequential Fe extraction schemes. Furthermore, even if published paleo-environmental reconstructions relied on well-preserved Fe

speciation data, stratigraphic variation in the data is most commonly interpreted to reflect temporal variation in seawater chemistry rather than spatial variability associated with a change in the depositional environment. Our modern marine data compilation reveals large spatial variability in Fe speciation at a fixed and well-characterized point in Earth history. This highlights the necessity to consider similar variability in past environments and its implications for interpretation of stratigraphic variation in Fe speciation data. Finally, the geologic record comes mostly from continental margins and slopes (e.g., Peters and Husson, 2017). These depositional environments host many of the water-column and diagenetic (bio)geochemical processes that impact Fe speciation, and more generally, elemental cycling in the ocean. However, these environments are not representative of the majority of the ocean's volume and area, and it seems optimistic to be able to confidently extrapolate data from shallow marine sedimentary rocks to reconstruct the past chemistry and oxidation state of the ocean as a whole.

#### 4.4. Using $Fe_{HR}/Fe_T$ to constrain local Fe sources

Mass balance dictates that steady-state  $Fe_{HR}/Fe_T$  ratios at the leftmost end of Array 1 or along Array 2 converge on  $Fe_{HR}/Fe_T$  ratios in the local sediment source. Indeed, we observe close similarities between the lowest  $Fe_{HR}/Fe_T$  in Array 1 and/or the approximately constant  $Fe_{HR}/Fe_T$  in Array 2 and sources of Fe to the local depositional environment of cores deposited within 300 km of the Rhone, Waitaki, Mississippi, Danube and Yangtze rivers (Fig. S10). Hence, we suggest that geologic  $Fe_{HR}/Fe_T$  data may serve to constrain local Fe sources. If confirmed by further studies, these constraints are expected to be robust to any alteration process that does not involve transformation of reactive to unreactive Fe or vice versa. Among these processes are diagenetic and metasomatic pyrite formation that does not involve the release of extra Fe (i.e., along Array 2), and pyrite oxidation during exhumation, exposure, sampling, or storage.

Processes that are expected to compromise  $Fe_{HR}/Fe_T$ -based constraints on the local Fe source include metamorphic or diagenetic formation of Fe-bearing silicates. These processes transfer Fe from reactive minerals ((oxyhydr)oxides, sulfides, carbonates) to more slowly reacting minerals (silicates), thereby decreasing  $Fe_{HR}/Fe_T$ . In contrast, extra Fe pyritization transfers Fe from the poorly reactive pool to the reactive pool, and  $Fe_{HR}/Fe_T$  increases. Extra Fe pyritization and some of the Fe silicate-forming processes may be identified by covariation between  $Fe_{HR}/Fe_T$  and  $Fe_{PYR}/Fe_{HR}$  (e.g., along Array 3). If sampling frequency precludes the construction of arrays in Fe speciation space, based on the four cores measured in this study, we suggest low bulk  $\delta^{34}S_{PYR}$  values as possible indicators of pyrite that did not form in association with extra Fe release (Fig. 7B). Low  $\delta^{34}S_{PYR}$  values (i.e., offset by  $\geq 40$ –50‰ from coeval estimates of seawater  $\delta^{34}S$ ) are expected along Array 2 and indicate a lesser degree of isotopic distillation, possibly during the earlier stages of diagenesis, before extra Fe pyritization occurs. Lastly, careful petrographic work may reveal late-stage shifts of Fe between the reactive and poorly reactive pools.

If robust global geologic records of  $Fe_{HR}/Fe_T$  in local Fe sources can be constructed on the basis of the above guidelines (no  $Fe_{HR}/Fe_T$ - $Fe_{PYR}/Fe_{HR}$  covariation, low  $\delta^{34}S_{PYR}$  values, no petrographic evidence of Fe shifts between pools), one might expect lower  $Fe_{HR}/Fe_T$  early in Earth history. With progressive oxygenation of the atmosphere, increasingly effective oxidative weathering is expected to have increased the proportion of Fe (oxyhydr)oxides relative to Fe silicates in suspended river sediments (Slotznick et al., 2018b). Additionally, with increasing atmospheric  $O_2$  levels and decreasing seawater silica concentrations in response to the evolution of silicifying organisms, the formation of Fe-bearing

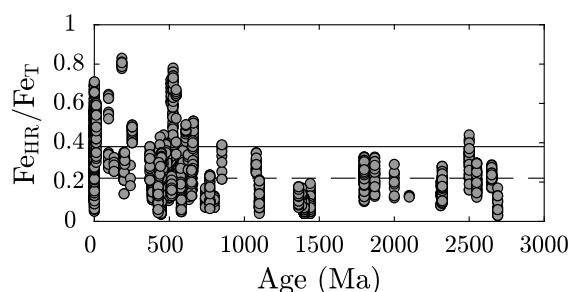


**Fig. 10.**  $Fe_{HR}/Fe_T$  in modern sediments and sedimentary rocks that display Array 2 variations in Fe speciation (i.e.,  $Fe_{PYR}/Fe_{HR}$  increase with little or no change in the average  $Fe_{HR}/Fe_T$ ). The variation in  $Fe_{PYR}/Fe_{HR}$  is interpreted to reflect progressive sulfidization of reactive Fe species.

authigenic clays (reverse weathering) is thought to have decreased in the early Paleozoic (Isson and Planavsky, 2018). The decrease in the delivery of Fe-bearing silicates in rivers and in Fe silicate authigenesis in marine sediments is expected to have led to progressively higher  $Fe_{HR}/Fe_T$  in marine sedimentary rocks over time. Though  $\delta^{34}S_{PYR}$  values are available for only some of the samples in our literature compilation, and petrographic information is almost entirely unavailable, we curated the compilation to include only samples that appear to be on Array 2 in a  $Fe_{HR}/Fe_T$ - $Fe_{PYR}/Fe_{HR}$  field (i.e., where Fe transfer between its reactive and poorly reactive pools is not expected). As metamorphism is unlikely to shift  $Fe_{HR}/Fe_T$  in all samples in a section by the same amount, the inclusion of samples only on Array 2 decreases the probability that the curated dataset is substantially affected by metamorphism. The curated dataset shows a Neoproterozoic-Cambrian increase in the range of  $Fe_{HR}/Fe_T$  (Fig. 10), in accordance with the expectations discussed above. It is not possible to confidently identify the relative importance of an increase in the efficiency of oxidative Fe-silicate weathering or a decrease in reverse weathering rates as the drivers of the apparent increase in  $Fe_{HR}/Fe_T$ .

## 5. Conclusions

The speciation of sequentially extracted Fe in sedimentary rocks has been widely used to constrain the chemistry and oxidation state of Earth's oceans over time. This approach was based on a relatively small dataset ( $n = 255$ ) of modern marine surface sediments (Raiswell and Canfield, 1998). Though all sedimentary rocks in which Fe speciation measurements were made have undergone diagenesis, the effects of diagenesis on the preserved Fe speciation have not been systematically studied. A more recent and larger ( $n = 1068$ ) survey of Fe speciation in modern marine sediments still included mostly surface sediments (Hardisty et al., 2018), and insights into the effects of diagenesis on Fe speciation have thus remained limited. We compiled and curated data from 316 long boreholes in which Fe speciation measurements were made ( $n = 2990$ ). The compilation included locations in which the sediments were deposited under oxic, low- $O_2$ , ferruginous and euxinic water columns. The inclusion of buried sediments in the compilation, not only surface sediments, allowed systematic investigation of the effects of diagenesis on Fe speciation.

In surficial sediments, we do observe a higher median  $Fe_{PYR}/Fe_{HR}$  in association with euxinic water columns ( $\approx 0.53$ ) than with oxic or low- $O_2$  water columns ( $\approx 0.1$ ), as found in previous studies. However,  $Fe_{PYR}/Fe_{HR}$  in the surficial sediments underlying euxinic water columns spans a wide range between 0 and  $\approx 0.8$ , and most of these surficial sediments ( $\approx 75\%$ ) display  $Fe_{PYR}/Fe_{HR}$  that would incorrectly classify them as oxic (i.e.,  $< 0.7$ ; Fig. 2C). When including buried sediments (depth  $> 2$  cm), our compilation reveals that between  $\approx 50\%$  and  $\approx 80\%$  of samples inhabit an “incorrect” part

of the  $Fe_{HR}/Fe_T-Fe_{PYR}/Fe_{HR}$  field, depending on the  $Fe_{HR}/Fe_T$  threshold used to distinguish oxic from anoxic environments (0.22 or 0.38) and the  $Fe_{PYR}/Fe_{HR}$  threshold used to distinguish ferruginous from euxinic environments (0.7 or 0.8).

Our results allow exploration of the evolution of Fe speciation during diagenesis, and on this basis, we suggest that the incorrect classifications stem from the effects of diagenesis on Fe speciation. Specifically,  $Fe_{HR}/Fe_T-Fe_{PYR}/Fe_{HR}$  data are generally observed to vary along three types of arrays (Fig. 4B), which are linked to different diagenetic processes. We suggest that variation along Array 1, which is typically encountered in the shallow sediments, represents mobilization of Fe by reductive dissolution of Fe(III) (oxyhydr)oxides near the sediment–water interface and subsequent oxidation of the dissolved  $Fe^{2+}$  at the oxycline. Array 2 (increase in  $Fe_{PYR}/Fe_{HR}$  and no change in  $Fe_{HR}/Fe_T$ ) represents sulfidization of readily reactive Fe species, such as oxides and oxyhydroxides, and Array 3 (positive  $Fe_{HR}/Fe_T-Fe_{PYR}/Fe_{HR}$  covariation) represents sulfidization either of progressively less reactive Fe-bearing phases (e.g., silicates) or of exogenously sourced Fe (e.g., effects of methane production and consumption on Fe(III)-bearing minerals at and/or below the sulfate-methane transition zone). The three modes of  $Fe_{HR}/Fe_T-Fe_{PYR}/Fe_{HR}$  covariation typically occur at different depths within the sediment, with Array 1 present mostly close to the sediment–water interface and Array 3 appearing deepest within the sediments. This order of appearance is expected, given the typical order of proposed processes responsible for generating the different covariations. Our results then suggest that stratigraphic variation in Fe speciation may in many cases represent progressive burial rather than variation in water-column chemistry.

Based on the above, we suggest that Fe speciation in marine sediments and sedimentary rocks, if well preserved, represents mostly the early diagenetic conditions rather than water-column chemistry and oxidation state. This holds irrespective of whether Fe speciation data are in the form of stratigraphic variation in a single location, an average in a single location, or the statistics of many different locations binned in time or space. Furthermore, late-stage alteration may compromise the Fe speciation acquired during diagenesis. For example, metamorphism may shift Fe from its reactive pools to unreactive phases (decreasing  $Fe_{HR}/Fe_T$ ), whereas oxidation during exposure, storage and/or sampling may shift Fe from the pyrite to the non-pyrite reactive pool (decreasing  $Fe_{PYR}/Fe_{HR}$ ). Such alteration complicates interpretations of Fe speciation data.

We suggest that  $Fe_{HR}/Fe_T$  in many marine sediments and sedimentary rocks, if primary, may be used to constrain the  $Fe_{HR}/Fe_T$  in the local sediment source, even when considering the diagenetic controls on Fe speciation. Specifically,  $Fe_{HR}/Fe_T$  in sample suites that display progressive sulfidization of reactive Fe species (i.e., the lowermost  $Fe_{HR}/Fe_T$  in Array 1 and the average  $Fe_{HR}/Fe_T$  in Array 2) are expected to resemble the sediment source. Samples that indicate extra-Fe sulfidization (i.e., along Array 3) or those in which Fe has been shifted between its reactive and unreactive pools (e.g., by metamorphism) may not be used to reconstruct the  $Fe_{HR}/Fe_T$  in the local sediment source. We suggest that the existence of Array 2-type variation, low pyrite  $\delta^{34}S$  values, and petrographic evidence for the absence of Fe transfer into silicate phases are indicative of  $Fe_{HR}/Fe_T$  values that represent the local sediment source. Though petrographic and sulfur isotopic data do not exist for most of the samples in our compilation, by screening to include only data along occurrences of Array 2, we find a possible increase in  $Fe_{HR}/Fe_T$  over Earth history. Such an increase is expected if atmospheric  $O_2$  levels increased, and seawater silica concentrations decreased over time. These secular changes in the chemistry of Earth's surface environment may be expected to cause increasingly efficient oxidative weathering of silicate rocks

on land and a reverse weathering Fe sink of decreasing importance, both of which favor preservation of higher  $Fe_{HR}/Fe_T$ .

In summary, the speciation of Fe-bearing phases in marine sediments and sedimentary rocks reflects the local/regional Fe source, depositional properties, diagenetic processes, metamorphism, and late-stage alteration. Considering these multiple controls on Fe speciation, interpretations of  $Fe_{HR}/Fe_T-Fe_{PYR}/Fe_{HR}$  data within the accepted framework, which is based on modern surface sediments and does not account for the effects of diagenesis, often yield incorrect insight into ancient depositional environments and waters. Petrographic, mineralogical, and complementary geochemical constraints, when used with the understanding of the multiple controls on Fe speciation described in this study, may allow the use of Fe speciation data to constrain the Fe source and the mode of diagenesis, but almost never the chemistry or oxidation state of the water column.

### Declaration of Competing Interest

The authors declare that they have no known competing financial interests or personal relationships that could have appeared to influence the work reported in this paper.

### Data availability

Data provide as Supplementary Materials

### Acknowledgments

We acknowledge helpful discussions with Nir Galili, Peter Crockford and Shahar Hegyi. V.P. acknowledges a Dean of the Chemistry Faculty Postdoctoral Fellowship from the Weizmann Institute of Science. I.H. acknowledges a Starting Grant from the European Research Council (No. 755053).

### Appendix A. Supplementary material

Supplementary material to this article can be found online at <https://doi.org/10.1016/j.gca.2022.08.037>.

### References

- Aeppli, M., Giroud, S., Vranic, S., Voegelin, A., Hofstetter, T.B., Sander, M., 2022. Thermodynamic controls on rates of iron oxide reduction by extracellular electron shuttles. *Proc. Natl. Acad. Sci. U. S. A.* 119. e2115629119.
- Ahm, A.-S.-C., Bjerrum, C.J., Hammarlund, E.U., 2017. Disentangling the record of diagenesis, local redox conditions, and global seawater chemistry during the latest Ordovician glaciation. *Earth Planet. Sci. Lett.* 459, 145–156.
- Aller, R.C., 2014. 8.11 – Sedimentary Diagenesis, Depositional Environments, and Benthic Fluxes. In: Heinrich, D., Holland, K.K.T. (Eds.), *Treatise on Geochemistry*, second ed. Elsevier, pp. 293–334.
- Aller, R.C., Madrid, V., Chistoserdov, A., Aller, J.Y., Heilbrun, C., 2010. Unsteady diagenetic processes and sulfur biogeochemistry in tropical deltaic muds: Implications for oceanic isotope cycles and the sedimentary record. *Geochim. Cosmochim. Acta* 74, 4671–4692.
- Anderson, T.F., Raiswell, R., 2004. Sources and mechanisms for the enrichment of highly reactive iron in euxinic black sea sediments. *Am. J. Sci.* 304, 203–233.
- Aquilina, A., Homoky, W.B., Hawkes, J.A., Lyons, T.W., Mills, R.A., 2014. Hydrothermal sediments are a source of water column Fe and Mn in the Bransfield Strait, Antarctica. *Geochim. Cosmochim. Acta* 137, 64–80.
- Asael, D., Tissot, F.L.H., Reinhard, C.T., Rouxel, O., Dauphas, N., Lyons, T.W., Ponzevera, E., Liorzou, C., Chéron, S., 2013. Coupled molybdenum, iron and uranium stable isotopes as oceanic paleoredox proxies during the Paleoproterozoic Shunga Event. *Chem. Geol.* 362, 193–210.
- Beal, E.J., House, C.H., Orphan, V.J., 2009. Manganese- and iron-dependent marine methane oxidation. *Science* 325, 184–187.
- Benkovitz, A., Matthews, A., Teutsch, N., Poulton, S.W., Bar-Matthews, M., Almgö-Labin, A., 2020. Tracing water column euxinia in Eastern Mediterranean Sapropels S5 and S7. *Chem. Geol.* 545, 119627.

- Berner, R.A., 1964. An idealized model of dissolved sulfate distribution in recent sediments. *Geochim. Cosmochim. Acta* 28, 1497–1503.
- Berner, R.A., 1981. A new geochemical classification of sedimentary environments. *J. Sediment. Res.* 51, 359–365.
- Berner, R.A., 1984. Sedimentary pyrite formation – An update. *Geochim. Cosmochim. Acta* 48, 605–615.
- Bond, D.P.G., Grasby, S.E., 2017. On the causes of mass extinctions. *Palaeogeography, Palaeoclimatology, Palaeoecology* 478, 3–29.
- Bosco-Santos, A., Gilhooly, W.P., Fouskas, F., Fabricio-Silva, W., Oliveira, E.P., 2020. Euxinia in the Neoproterozoic: The starting point for early oxygenation in a Brazilian Craton. *Precamb. Res.* 341, 105655.
- Bowman, C.N., Them, T.R., Knight, M.D., Kaljo, D., Eriksson, M.E., Hints, O., Martma, T., Owens, J.D., Young, S.A., 2021. A multi-proxy approach to constrain reducing conditions in the Baltic Basin during the late Silurian Lau carbon isotope excursion. *Palaeogeogr. Palaeoclimatol. Palaeoecol.* 581, 110624.
- Canfield, D.E., 1989. Reactive iron in marine sediments. *Geochim. Cosmochim. Acta* 53, 619–632.
- Canfield, D.E., Berner, R.A., 1987. Dissolution and pyritization of magnetite in anoxic marine sediments. *Geochim. Cosmochim. Acta* 51, 645–659.
- Canfield, D.E., Raiswell, R., Westrich, J.T., Reaves, C.M., Berner, R.A., 1986. The use of chromium reduction in the analysis of reduced inorganic sulfur in sediments and shales. *Chem. Geol.* 54, 149–155.
- Canfield, D.E., Raiswell, R., Bottrell, S.H., 1992. The reactivity of sedimentary iron minerals toward sulfide. *Am. J. Sci.* 292, 659–683.
- Canfield, D.E., Lyons, T., Raiswell, R., 1996. A model for iron deposition to euxinic black sea sediments. *Am. J. Sci.* 296, 818–834.
- Carter, R.M., McCave, I.N., Richter, C., Carter, L., 1999. 7. Site 1123 North Chatham Drift – a 20-Ma Record of the Pacific Deep Western Boundary Current. *Proc. Ocean Drilling Programs, Initial Rep.* 181, 1–184.
- Clarkson, M.O., Poulton, S.W., Guilbaud, R., Wood, R.A., 2014. Assessing the utility of Fe/Al and Fe-speciation to record water column redox conditions in carbonate-rich sediments. *Chem. Geol.* 382, 111–122.
- Cole, D.B., Reinhard, C.T., Wang, X., Gueguen, B., Halverson, G.P., Gibson, T., Hodgskiss, M.S.W., McKenzie, N.R., Lyons, T.W., Planavsky, N.J., 2016. A shale-hosted Cr isotope record of low atmospheric oxygen during the Proterozoic. *Geology* 44, 555–558.
- Contreras, S., Meister, P., Liu, B., Prieto-Mollar, X., Hinrichs, K.U., Khalili, A., Ferdelman, T.G., Kuypers, M.M., Jørgensen, B.B., 2013. Cyclic 100-ka (glacial-interglacial) migration of subseafloor redox zonation on the Peruvian shelf. *Proc. Natl. Acad. Sci. U. S. A.* 110, 18098–18103.
- D'Hondt, S.L., Jørgensen, B.B., Miller, D.J., 2003. Shipboard Scientific Party, 2003. Site 1229. *Proceedings of the ocean Drilling Programs, Initial Reports* 201, 1–78.
- Dale, A.W., Brüchert, V., Alperin, M., Regnier, P., 2009. An integrated sulfur isotope model for Namibian shelf sediments. *Geochim. Cosmochim. Acta* 73, 1924–1944.
- D'Hondt, S., Rutherford, S., Spivack, A.J., 2002. Metabolic activity of subsurface life in deep-sea sediments. *Science* 295, 2067–2070.
- Dijkstra, N., Slomp, C.P., Behrends, T., 2016. Vivianite is a key sink for phosphorus in sediments of the Landsort Deep, an intermittently anoxic deep basin in the Baltic Sea. *Chem. Geol.* 438, 58–72.
- Doyle, K.A., Poulton, S.W., Newton, R.J., Podkovyrov, V.N., Bekker, A., 2018. Shallow water anoxia in the Mesoproterozoic ocean: Evidence from the Bashkir Meganticlinorium, Southern Urals. *Precamb. Res.* 317, 196–210.
- Durrieu De Madron, X., Abassi, A., Heussner, S., Monaco, A., Aloisi, J.C., Radakovitch, O., Giresse, P., Buscail, R., Kerherve, P., 2000. Particulate matter and organic carbon budgets for the Gulf of Lions (NW Mediterranean). *Oceanol. Acta* 23, 717–730.
- Egger, M., Jilbert, T., Behrends, T., Rivard, C., Slomp, C.P., 2015a. Vivianite is a major sink for phosphorus in methanogenic coastal surface sediments. *Geochim. Cosmochim. Acta* 169, 217–235.
- Egger, M., Rasigraf, O., Sapart, C.J., Jilbert, T., Jetten, M.S., Rockmann, T., van der Veen, C., Banda, N., Kartal, B., Ettwig, K.F., Slomp, C.P., 2015b. Iron-mediated anaerobic oxidation of methane in brackish coastal sediments. *Environ. Sci. Technol.* 49, 277–283.
- Egger, M., Kraal, P., Jilbert, T., Sulu-Gambari, F., Sapart, C.J., Röckmann, T., Slomp, C.P., 2016. Anaerobic oxidation of methane alters sediment records of sulfur, iron and phosphorus in the Black Sea. *Biogeosciences* 13, 5333–5355.
- Eroglu, S., Scholz, F., Salvatelli, R., Siebert, C., Schneider, R., Frank, M., 2021. The impact of postdepositional alteration on iron- and molybdenum-based redox proxies. *Geology* 49, 1411–1415.
- Farquhar, J., Bao, H., Thiemens, M., 2000. Atmospheric influence of Earth's earliest sulfur cycle. *Science* 289, 756–759.
- Fernandes, S., Mazumdar, A., Peketi, A., Anand, S.S., Rengarajan, R., Jose, A., Manaskanya, A., Carvalho, M.A., Shetty, D., 2020. Sulfidization processes in seasonally hypoxic shelf sediments: A study off the West coast of India. *Mar. Pet. Geol.* 117, 104353.
- Fike, D.A., Bradley, A.S., Rose, C.V., 2015. Rethinking the Ancient Sulfur Cycle. *Annu. Rev. Earth Planet. Sci.* 43, 593–622.
- Froelich, P.N., Klinkhammer, P., Bender, M.L., Luedtke, N.A., Heath, G.R., Cullen, D., Dauphin, P., 1979. Early oxidation of organic matter in pelagic sediments of the eastern equatorial Atlantic: suboxic diagenesis. *Geochim. Cosmochim. Acta* 43, 1075–1090.
- Fulthorpe, C.S., Hoyanagi, K., Blum, P., 2011. IODP Expedition 317: Exploring the Record of Sea-Level Change Off New Zealand. *Sci. Drill.* 12, 4–14.
- Gartman, A., Luther, G.W., 2014. Oxidation of synthesized sub-micron pyrite (FeS<sub>2</sub>) in seawater. *Geochim. Cosmochim. Acta* 144, 96–108.
- Gilleaudeau, G.J., Kah, L.C., 2015. Heterogeneous redox conditions and a shallow chemocline in the Mesoproterozoic ocean: Evidence from carbon–sulfur–iron relationships. *Precamb. Res.* 257, 94–108.
- Goldberg, T., Archer, C., Vance, D., Thamdrup, B., McAnena, A., Poulton, S.W., 2012. Controls on Mo isotope fractionations in a Mn-rich anoxic marine sediment, Gullmar Fjord, Sweden. *Chem. Geol.* 296–297, 73–82.
- Gu, X., Heaney, P.J., Reis, F., Brantley, S.L., 2020a. Deep abiotic weathering of pyrite. *Science* 370, abb8092.
- Gu, X., Rempe, D.M., Dietrich, W.E., West, A.J., Lin, T.-C., Jin, L., Brantley, S.L., 2020b. Chemical reactions, porosity, and microfracturing in shale during weathering: The effect of erosion rate. *Geochim. Cosmochim. Acta* 269, 63–100.
- Guilbaud, R., Poulton, S.W., Butterfield, N.J., Zhu, M., Shields-Zhou, G.A., 2015. A global transition to ferruginous conditions in the early Neoproterozoic oceans. *Nat. Geosci.* 8, 466–470.
- Hardisty, D.S., Lu, Z., Planavsky, N.J., Bekker, A., Philippot, P., Zhou, X., Lyons, T.W., 2014. An iodine record of Paleoproterozoic surface ocean oxygenation. *Geology* 42, 619–622.
- Hardisty, D.S., Lyons, T.W., Riedinger, N., Isson, T.T., Owens, J.D., Aller, R.C., Rye, D.M., Planavsky, N.J., Reinhard, C.T., Gill, B.C., Masterson, A.L., Asael, D., Johnston, D.T., 2018. An evaluation of sedimentary molybdenum and iron as proxies for pore fluid paleoredox conditions. *Am. J. Sci.* 318, 527–556.
- Heitmann, T., Blodau, C., 2006. Oxidation and incorporation of hydrogen sulfide by dissolved organic matter. *Chem. Geol.* 235, 12–20.
- Hellige, K., Pollok, K., Larese-Casanova, P., Behrends, T., Peiffer, S., 2012. Pathways of ferrous iron mineral formation upon sulfidation of lepidocrocite surfaces. *Geochim. Cosmochim. Acta* 81, 69–81.
- Henkel, S., Kasten, S., Poulton, S.W., Staubwasser, M., 2016. Determination of the stable iron isotopic composition of sequentially leached iron phases in marine sediments. *Chem. Geol.* 421, 93–102.
- Henkel, S., Kasten, S., Hartmann, J.F., Silva-Busso, A., Staubwasser, M., 2018. Iron cycling and stable Fe isotope fractionation in Antarctic shelf sediments, King George Island. *Geochim. Cosmochim. Acta* 237, 320–338.
- Hepburn, L.E., Butler, I.B., Boyce, A., Schröder, C., 2020. The use of operationally-defined sequential Fe extraction methods for mineralogical applications: A cautionary tale from Mössbauer spectroscopy. *Chem. Geol.* 543, 119584.
- Hutchings, A.M., Turchyn, A.V., 2021. A quantification of the effect of diagenesis on the paleoredox record in mid-Proterozoic sedimentary rocks. *Geology* 49, 1143–1147.
- Isson, T.T., Planavsky, N.J., 2018. Reverse weathering as a long-term stabilizer of marine pH and planetary climate. *Nature* 560, 471–475.
- Jenkyns, H.C., 2010. Geochemistry of oceanic anoxic events. *Geochemistry, Geophysics, Geosystems* 11, n/a–n/a. <https://doi.org/10.1029/2009GC002788>.
- Jiang, S., Park, S., Yoon, Y., Lee, J.H., Wu, W.M., Phuoc Dan, N., Sadowsky, M.J., Hur, H. G., 2013. Methanogenesis facilitated by geobiochemical iron cycle in a novel syntrophic methanogenic microbial community. *Environ. Sci. Technol.* 47, 10078–10084.
- Johnson, J.E., Gerpheide, A., Lamb, M.P., Fischer, W.W., 2014. O<sub>2</sub> constraints from Paleoproterozoic detrital pyrite and uraninite. *Geol. Soc. Am. Bull.* 126, 813–830.
- Jørgensen, B.B., Beulig, F., Egger, M., Petro, C., Scholze, C., Røy, H., 2019. Organoclastic sulfate reduction in the sulfate-methane transition of marine sediments. *Geochim. Cosmochim. Acta* 254, 231–245.
- Jørgensen, B.B., Findlay, A.J., Pellerin, A., 2019. The Biogeochemical Sulfur Cycle of Marine Sediments. *Front. Microbiol.* 10, 849.
- Kah, L.C., Lyons, T.W., Frank, T.D., 2004. Low marine sulphate and protracted oxygenation of the Proterozoic biosphere. *Nature* 431, 834–838.
- Kanzaki, Y., Murakami, T., 2015. Estimates of atmospheric CO<sub>2</sub> in the Neoproterozoic-Paleoproterozoic from paleosols. *Geochim. Cosmochim. Acta* 159, 190–219.
- Kato, S., Hashimoto, K., Watanabe, K., 2012. Methanogenesis facilitated by electric syntrophy via (semi)conductive iron-oxide minerals. *Environ. Microbiol.* 14, 1646–1654.
- Kemeny, P.C., Lopez, G.I., Dalleska, N.F., Torres, M., Burke, A., Bhatt, M.P., West, A.J., Hartmann, J., Adkins, J.F., 2021a. Sulfate sulfur isotopes and major ion chemistry reveal that pyrite oxidation counteracts CO<sub>2</sub> drawdown from silicate weathering in the Langtang-Trisuli-Narayani River system, Nepal Himalaya. *Geochim. Cosmochim. Acta* 294, 43–69.
- Kemeny, P.C., Torres, M.A., Lamb, M.P., Webb, S.M., Dalleska, N., Cole, T., Hou, Y., Marske, J., Adkins, J.F., Fischer, W.W., 2021b. Organic sulfur fluxes and geomorphic control of sulfur isotope ratios in rivers. *Earth Planet. Sci. Lett.* 562, 116838.
- Kraal, P., Dijkstra, N., Behrends, T., Slomp, C.P., 2017. Phosphorus burial in sediments of the sulfidic deep Black Sea: Key roles for adsorption by calcium carbonate and apatite authigenesis. *Geochim. Cosmochim. Acta* 204, 140–158.
- Kraal, P., Yücel, M., Slomp, C.P., 2019. Turbidite deposition and diagenesis in the southwestern Black Sea: Implications for biogeochemical cycling in an anoxic basin. *Mar. Chem.* 209, 48–61.
- Kubeneck, L.J., Lenstra, W.K., Malkin, S.Y., Conley, D.J., Slomp, C.P., 2021. Phosphorus burial in vivianite-type minerals in methane-rich coastal sediments. *Mar. Chem.* 119584.
- Lenstra, W.K., Hermans, M., Séguret, M.J.M., Witbaard, R., Behrends, T., Dijkstra, N., van Helmond, N.A.G.M., Kraal, P., Laan, P., Rijkenberg, M.J.A., Severmann, S., Teacă, A., Slomp, C.P., 2019. The shelf-to-basin iron shuttle in the Black Sea revisited. *Chem. Geol.* 511, 314–341.
- Lenstra, W.K., Hermans, M., Séguret, M.J.M., Witbaard, R., Severmann, S., Behrends, T., Slomp, C.P., 2020. Coastal hypoxia and eutrophication as key controls on benthic release and water column dynamics of iron and manganese. *Limnol. Oceanogr.* 66, 807–826.

- Li, X., Cutter, G.A., Thunell, R.C., Tappa, E., Gilhooly, W.P., Lyons, T.W., Astor, Y., Scranton, M.I., 2011. Particulate sulfur species in the water column of the Cariaco Basin. *Geochim. Cosmochim. Acta* 75, 148–163.
- Li, J., Li, L., Bai, S., Ta, K., Xu, H., Chen, S., Pan, J., Li, M., Du, M., Peng, X., 2019. New insight into the biogeochemical cycling of methane, S and Fe above the Sulfate-Methane Transition Zone in methane hydrate-bearing sediments: A case study in the Dongsha area, South China Sea. *Deep Sea Res. Part I* 145, 97–108.
- Liu, J., Pellerin, A., Antler, G., Kasten, S., Findlay, A.J., Dohrmann, I., Røy, H., Turchyn, A.V., Jørgensen, B.B., 2020. Early diagenesis of iron and sulfur in Bornholm Basin sediments: The role of near-surface pyrite formation. *Geochim. Cosmochim. Acta* 284, 43–60.
- Lu, W., Zhao, W., Balsam, W., Lu, H., Liu, P., Lu, Z., Ji, J., 2017. Iron Mineralogy and Speciation in Clay-Sized Fractions of Chinese Desert Sediments. *Journal of Geophysical Research: Atmospheres* 122, 13458–13471.
- Lyons, T., 1996. Sulfur isotopic trends and pathways of iron sulfide formation in upper Holocene sediments of the anoxic Black Sea. *Geochim. Cosmochim. Acta* 61, 3367–3382.
- Lyons, T.W., Severmann, S., 2006. A critical look at iron paleoredox proxies: New insights from modern euxinic marine basins. *Geochim. Cosmochim. Acta* 70, 5698–5722.
- Ma, W.-W., Zhu, M.-X., Yang, G.-P., Li, T., 2018. Iron geochemistry and organic carbon preservation by iron (oxyhydr)oxides in surface sediments of the East China Sea and the south Yellow Sea. *J. Mar. Syst.* 178, 62–74.
- Mahoney, C., März, C., Buckman, J., Wagner, T., Blanco-Velandia, V.-O., 2019. Pyrite oxidation in shales: Implications for palaeo-redox proxies based on geochemical and SEM-EDX evidence. *Sed. Geol.* 389, 186–199.
- März, C., Poulton, S.W., Beckmann, B., Küster, K., Wagner, T., Kasten, S., 2008. Redox sensitivity of P cycling during marine black shale formation: Dynamics of sulfidic and anoxic, non-sulfidic bottom waters. *Geochim. Cosmochim. Acta* 72, 3703–3717.
- Matthews, A., Azrieli-Tal, I., Benkovitz, A., Bar-Matthews, M., Vance, D., Poulton, S. W., Teutsch, N., Almogi-Labin, A., Archer, C., 2017. Anoxic development of sapropel S1 in the Nile Fan inferred from redox sensitive proxies, Fe speciation, Fe and Mo isotopes. *Chem. Geol.* 475, 24–39.
- Meister, P., Brunner, B., Picard, A., Bottcher, M.E., Jørgensen, B.B., 2019. Sulphur and carbon isotopes as tracers of past sub-seafloor microbial activity. *Sci. Rep.* 9, 604.
- Mossmann, J., Aplin, A.C., Curtis, C., Coleman, M.L., 1991. Geochemistry of inorganic and organic sulphur in organic-rich sediment from the Peru margin. *Geochim. Cosmochim. Acta* 55, 3581–3595.
- Nguyen, K., Love, G.D., Zumberge, J.A., Kelly, A.E., Owens, J.D., Rohrsen, M.K., Bates, S.M., Cai, C., Lyons, T.W., 2019. Absence of biomarker evidence for early eukaryotic life from the Mesoproterozoic Roper Group: Searching across a marine redox gradient in mid-Proterozoic habitability. *Geobiology* 17, 247–260.
- Noröi, K.A., Thamdrup, B., Schubert, C.J., 2013. Anaerobic oxidation of methane in an iron-rich Danish freshwater lake sediment. *Limnol. Oceanogr.* 58, 546–554.
- Partin, C.A., Bekker, A., Planavsky, N.J., Scott, C.T., Gill, B.C., Li, C., Podkovyrov, V., Maslov, A., Konhauser, K.O., Lalonde, S.V., Love, G.D., Poulton, S.W., Lyons, T.W., 2013. Large-scale fluctuations in Precambrian atmospheric and oceanic oxygen levels from the record of U in shales. *Earth Planet. Sci. Lett.* 369–370, 284–293.
- Partin, C.A., Bekker, A., Planavsky, N.J., Lyons, T.W., 2015. Euxinic conditions recorded in the ca. 1.93 Ga Bravo Lake Formation, Nunavut (Canada): Implications for oceanic redox evolution. *Chem. Geol.* 417, 148–162.
- Pasquier, V., Sansjofre, P., Rabineau, M., Révillon, S., Houghton, J., Fike, D.A., 2017. Pyrite sulfur isotopes reveal glacial-interglacial environmental changes. *Proc. Natl. Acad. Sci. U. S. A.* 114, 5941–5945.
- Pasquier, V., Bryant, R.N., Fike, D.A., Halevy, I., 2021a. Strong local, not global, controls on marine pyrite sulfur isotopes. *Sci. Adv.* 7, eabb7403.
- Pasquier, V., Fike, D.A., Halevy, I., 2021b. Sedimentary pyrite sulfur isotopes track the local dynamics of the Peruvian oxygen minimum zone. *Nat. Commun.* 12, 4403.
- Peiffer, S., Behrends, T., Hellige, K., Larese-Casanova, P., Wan, M., Pollok, K., 2015. Pyrite formation and mineral transformation pathways upon sulfidation of ferric hydroxides depend on mineral type and sulfide concentration. *Chem. Geol.* 400, 44–55.
- Peiffer, S., Gade, W., 2007. Reactivity of Ferric Oxides toward H<sub>2</sub>S at Low pH. *Environ. Sci. Technol.* 41, 3159–3164.
- Peketi, A., Mazumdar, A., Joshi, R.K., Patil, D.J., Srinivas, P.L., Dayal, A.M., 2012. Tracing the Paleo sulfate-methane transition zones and H<sub>2</sub>S seepage events in marine sediments: An application of C-S-Mo systematics. *Geochim. Geophys. Geosyst.* 13, Q10007.
- Pellerin, A., Antler, G., Røy, H., Findlay, A., Beulig, F., Scholze, C., Turchyn, A.V., Jørgensen, B.B., 2018. The sulfur cycle below the sulfate-methane transition of marine sediments. *Geochim. Cosmochim. Acta* 239, 74–89.
- Peters, S.E., Husson, J.M., 2017. Sediment cycling on continental and oceanic crust. *Geology* 45, 323–326.
- Poulton, S.W., Canfield, D.E., 2005. Development of a sequential extraction procedure for iron: implications for iron partitioning in continentally derived particulates. *Chem. Geol.* 214, 209–221.
- Poulton, S.W., Canfield, D.E., 2011. Ferruginous conditions: A dominant feature of the ocean through Earth's history. *Elements* 7, 107–112.
- Poulton, S.W., Krom, M.D., Raiswell, R., 2004. A revised scheme for the reactivity of iron (oxyhydr)oxide minerals towards dissolved sulfide. *Geochim. Cosmochim. Acta* 68, 3703–3715.
- Poulton, S.W., Fralick, P.W., Canfield, D.E., 2010. Spatial variability in oceanic redox structure 1.8 billion years ago. *Nat. Geosci.* 3, 486–490.
- Poulton, S.W., Raiswell, R., 2002. The low-temperature geochemical cycle of iron from continental fluxes to marine sediment deposition. *Am. J. Sci.* 302, 774–805.
- Rabineau, M., Leroux, E., Aslanian, D., Bache, F., Gorini, C., Moulin, M., Molliex, S., Droz, L., dos Reis, A.T., Rubino, J.L., Guillocheau, F., Olivet, J.L., 2014. Quantifying subsidence and isostatic readjustment using sedimentary paleomarkers, example from the Gulf of Lion. *Earth Planet. Sci. Lett.* 388, 353–366.
- Raiswell, R., Berner, R.A., 1986. Pyrite and organic matter in Phanerozoic normal marine shales. *Geochim. Cosmochim. Acta* 50, 1967–1976.
- Raiswell, R., Canfield, D.E., 1996. Rates of reaction between silicate iron and dissolved sulfide in Peru Margin sediments. *Geochim. Cosmochim. Acta* 60, 2777–2787.
- Raiswell, R., Canfield, D.E., 1998. Sources of iron for pyrite formation in marine sediments. *Am. J. Sci.* 298, 219–245.
- Raiswell, R., Canfield, D.E., 2012. The iron biogeochemical cycle Past and Present. *Geochemical Perspectives*, Paris.
- Raiswell, R., Tranter, M., Benning, L.G., Siegert, M., De'ath, R., Huybrechts, P., Payne, T., 2006. Contributions from glacially derived sediment to the global iron (oxyhydr)oxide cycle: Implications for iron delivery to the oceans. *Geochim. Cosmochim. Acta* 70, 2765–2780.
- Raiswell, R., Hardisty, D.S., Lyons, T.W., Canfield, D.E., Owens, J.D., Planavsky, N.J., Poulton, S.W., Reinhard, C.T., 2018. The iron paleoredox proxies: A guide to the pitfalls, problems and proper practice. *Am. J. Sci.* 318, 491–526.
- Raven, M.R., Sessions, A.L., Fischer, W.W., Adkins, J.F., 2016. Sedimentary pyrite  $\delta^{34}\text{S}$  differs from porewater sulfide in Santa Barbara Basin: Proposed role of organic sulfur. *Geochim. Cosmochim. Acta* 186, 120–134.
- Reinhard, C.T., Planavsky, N.J., Lyons, T.W., 2013. Long-term sedimentary recycling of rare sulphur isotope anomalies. *Nature* 497, 100–103.
- Reuschel, M., Melezhik, V.A., Strauss, H., 2012. Sulfur isotopic trends and iron speciation from the c. 2.0 Ga Pilgūjärvi Sedimentary Formation, NW Russia. *Precamb. Res.* 196–197, 193–203.
- Révillon, S., Jouet, G., Bayon, G., Rabineau, M., Dennielou, B., Hémond, C., Berné, S., 2011. The provenance of sediments in the Gulf of Lions, western Mediterranean Sea. *Geochem. Geophys. Geosyst.* 12, Q08006.
- Riboulot, V., Thomas, Y., Berné, S., Jouet, G., Cattaneo, A., 2014. Control of Quaternary sea-level changes on gas seeps. *Geophys. Res. Lett.* 41, 4970–4977.
- Rickard, D., 2012a. Iron Isotope Fractionation in Sedimentary Sulfides, Sulfidic Sediments and Sedimentary Rocks, pp. 475–493.
- Rickard, D., 2012b. Sedimentary Iron Biogeochemistry, Sulfidic Sediments and Sedimentary Rocks, pp. 85–119.
- Scholz, F., 2018. Identifying oxygen minimum zone-type biogeochemical cycling in Earth history using inorganic geochemical proxies. *Earth Sci. Rev.* 184, 29–45.
- Scholz, F., McManus, J., Mix, A.C., Hensen, C., Schneider, R.R., 2014a. The impact of ocean deoxygenation on iron release from continental margin sediments. *Nat. Geosci.* 7, 433–437.
- Scholz, F., Severmann, S., McManus, J., Noffke, A., Lomnitz, U., Hensen, C., 2014b. On the isotope composition of reactive iron in marine sediments: Redox shuttle versus early diagenesis. *Chem. Geol.* 389, 48–59.
- Scholz, F., Siebert, C., Dale, A.W., Frank, M., 2017. Intense molybdenum accumulation in sediments underneath a nitrogenous water column and implications for the reconstruction of paleo-redox conditions based on molybdenum isotopes. *Geochim. Cosmochim. Acta* 213, 400–417.
- Scholz, F., Schmidt, M., Hensen, C., Eroglu, S., Geilert, S., Gutjahr, M., Liebetrau, V., 2019. Shelf-to-basin iron shuttle in the Guaymas Basin, Gulf of California. *Geochim. Cosmochim. Acta* 261, 76–92.
- Shawar, L., Halevy, I., Said-Ahmad, W., Feinstein, S., Boyko, V., Kamyshtny, A., Amrani, A., 2018. Dynamics of pyrite formation and organic matter sulfuration in organic-rich carbonate sediments. *Geochim. Cosmochim. Acta* 241, 219–239.
- Sheldon, N.D., 2006. Precambrian paleosols and atmospheric CO<sub>2</sub> levels. *Precamb. Res.* 147, 148–155.
- Sheldon, N.D., Mitchell, R.L., Dzombak, R.M., 2021. Reconstructing Precambrian pCO<sub>2</sub> and pO<sub>2</sub> using paleosols.
- Sivan, O., Adler, M., Pearson, A., Gelman, F., Bar-Or, I., John, S.G., Eckert, W., 2011. Geochemical evidence for iron-mediated anaerobic oxidation of methane. *Limnol. Oceanogr.* 56, 1536–1544.
- Sivan, O., Antler, G., Turchyn, A.V., Marlow, J.J., Orphan, V.J., 2014. Iron oxides stimulate sulfate-driven anaerobic methane oxidation in seeps. *Proc. Natl. Acad. Sci. U. S. A.* 111, E4139–E4147.
- Sivan, O., Shusta, S.S., Valentine, D.L., 2016. Methanogens rapidly transition from methane production to iron reduction. *Geobiology* 14, 190–203.
- Slotznick, S.P., Eiler, J.M., Fischer, W.W., 2018a. The effects of metamorphism on iron mineralogy and the iron speciation redox proxy. *Geochim. Cosmochim. Acta* 224, 96–115.
- Slotznick, S.P., Swanson-Hysell, N.L., Sperling, E.A., 2018b. Oxygenated Mesoproterozoic lake revealed through magnetic mineralogy. *Proc. Natl. Acad. Sci. U. S. A.* 115, 12938–12943.
- Slotznick, S.P., Sperling, E.A., Tosca, N.J., Miller, A.J., Clayton, K.E., Helmond, N.A.G.M., Slomp, C.P., Swanson-Hysell, N.L., 2020. Unraveling the Mineralogical Complexity of Sediment Iron Speciation Using Sequential Extractions. *Geochim. Geophys. Geosyst.* 21, n/a.
- Sperling, E.A., Wolock, C.J., Morgan, A.S., Gill, B.C., Kunzmann, M., Halverson, G.P., Macdonald, F.A., Knoll, A.H., Johnston, D.T., 2015. Statistical analysis of iron

- geochemical data suggests limited late Proterozoic oxygenation. *Nature* 523, 451–454.
- Stolper, D.A., Keller, C.B., 2018. A record of deep-ocean dissolved O<sub>2</sub> from the oxidation state of iron in submarine basalts. *Nature* 553, 323–327.
- Stookey, L.L., 1970. Ferrozine—a new spectrophotometric reagent for iron. *Anal. Chem.* 42, 779–781.
- Turchyn, A.V., Sivan, O., Schrag, D.P., 2006. Oxygen isotopic composition of sulfate in deep sea pore fluid evidence for rapid sulfur cycling. *Geobiology* 4, 191–201.
- Vuillemin, A., Wirth, R., Kemnitz, H., Schleicher, A.M., Friese, A., Bauer, K.W., Simister, R., Nomosatryo, S., Ordoñez, L., Ariztegui, D., Henny, C., Crowe, S.A., Benning, L.G., Kallmeyer, J., Russell, J.M., Bijaksana, S., Vogel, H., 2019. Formation of diagenetic siderite in modern ferruginous sediments. *Geology* 47, 540–544.
- Walker, J.D., 2019. Geological timescale v. 5.0. Geological Society of America.
- Wan, M., Shchukarev, A., Lohmayer, R., Planer-Friedrich, B., Peiffer, S., 2014. Occurrence of surface polysulfides during the interaction between ferric (hydr) oxides and aqueous sulfide. *Environ. Sci. Technol.* 48, 5076–5084.
- Wan, M., Schröder, C., Peiffer, S., 2017. Fe(III):S(-II) concentration ratio controls the pathway and the kinetics of pyrite formation during sulfidation of ferric hydroxides. *Geochim. Cosmochim. Acta* 217, 334–348.
- Wan, J., Tokunaga, T.K., Williams, K.H., Dong, W., Brown, W., Henderson, A.N., Newman, A.W., Hubbard, S.S., 2019. Predicting sedimentary bedrock subsurface weathering fronts and weathering rates. *Sci. Rep.* 9, 17198.
- Wijsman, J.W.M., Middelburg, J.J., Heil, C.H.R., 2001. Reactive iron in Black Sea sediments Implications for iron cycling. *Mar. Geol.* 172, 167–180.
- Wilkin, R.T., Barnes, H.L., Brantley, S.L., 1996. The size distribution of framboidal pyrite in modern sediments: An indicator of redox conditions. *Geochim. Cosmochim. Acta* 60, 3897–3912.
- Wotte, T., Strauss, H., 2015. Questioning a widespread euxinia for the Furongian (Late Cambrian) SPICE event: indications from  $\delta^{13}\text{C}$ ,  $\delta^{18}\text{O}$ ,  $\delta^{34}\text{S}$  and biostratigraphic constraints. *Geol. Mag.* 152, 1085–1103.
- Zhuang, L., Xu, J., Tang, J., Zhou, S., 2015. Effect of ferrihydrite biomineralization on methanogenesis in an anaerobic incubation from paddy soil. *J. Geophys. Res. Biogeosci.* 120, 876–886.